UCB-NE-4220

LONG-TERM BEHAVIOUR OF BUFFER MATERIALS IN GEOLOGIC REPOSITORIES FOR HIGH-LEVEL WASTES

J. Verbeke, J. Ahn and P.L. Chambré

Department of Nuclear Engineering

University of California

Berkeley, California 94720

July 1997

The authors invite comments and would appreciate being notified of any errors in the report.

Joonhong Ahn
Department of Nuclear Engineering
University of California
Berkeley, CA 94720
USA

ahn@nuc.berkeley.edu

TABLE OF CONTENTS

3. GOVERNING EQUATIONS

4. SOLUTION FOR THE GOVERNING EQUATIONS

5. VALIDATION USING TERZAGHI'S ANALYTICAL SOLUTION

LIST OF FIGURES

LIST OF TABLES

AKNOWLEDGEMENTS

The research reported herein was supported by JGC Corporation, Japan, as part of a study on the geologic disposal system for the high-level radioactive waste, organized by the Central Research Institute for Electrical Power Industry (CRIEPI), Japan, and Tokyo Electric Power Industry Co., Japan.

CHAPTER
ONE

INTRODUCTION

1.1 GEOLOGIC REPOSITORIES

Many different possibilities have been considered for the long-term isolation of highly radioactive wastes from the environment, the goal being ultimately to decrease the amount of radioactivity released to the human beings. Among these different possibilities, the isolation of highly radioactive wastes in geologic formations is the one that has been retained by scientists. Considering the features of these repositories, some analyses have been performed to determine the possible scenarios that could lead to the release of radioactivity to the environment. Based on results of models or on common sense, many scenarios have been eliminated. Eventually, transport of radionuclides by groundwater from the waste emplacement to the environment has been retained as the most important scenario. The radionuclide transport by groundwater through the rock fractures depends on the hydrologic and chemical properties of this natural medium. These properties depend on the host rock and can thus hardly be modified. The release of radioactivity is thus mainly determined by the radionuclide travel length from the waste emplacement to the environment. In order to decrease this hazardous release, the stainless steel overcast containing the waste form is contained in a bentonite layer. Due to the very low permeability of the bentonite, the water movement is very slow in this layer and so is the radionuclide release.

1.2 MOTIVATION FOR THIS STUDY

With the bentonite as an engineered barrier, previous studies [1] showed that the total hazard would be reduced by a factor 100 at the bentonite/rock interface and by a factor 10,000 at 100 meters downstream. This shows the impact of the bentonite region on the radiological consequences. A remarkable property of the bentonite clay is its ability to swell by water absorption. As incoming groundwater flows through the rock fractures and wets the canister, the bentonite expands into the same fractures. As a result, the radionuclide travel time to the bentonite/rock interface is longer and by radioactive decay, the total hazard at this location decreases to even lower levels. Considering a model where a given length of the fractures intersecting the waste emplacement are filled with bentonite clay, previous studies showed [1] that the concentrations of americium, plutonium and neptunium reduce to negligible levels within the bentonite buffer region if the environment is reducing. The expanding bentonite region is thus a very effective barrier to the release of radioactive isotopes.

1.3 OBJECTIVE AND SUMMARY OF THIS STUDY

The goal of this project is to study the expansion of the bentonite through the fractures surrounding the bentonite. This project will be divided into three parts.

Chapter 2

In the first one, a survey of the literature is done to explain bentonite swelling by water absorption. Microscopic mechanisms of bentonite swelling are studied but neither the electrical double layer theory [2] nor the recently proposed hydration layer theory [3] gives a complete mechanistic explanation for clay swelling. On the other hand, macroscopic behavior of clay and soils have been analyzed successfully by the consolidation theory established by Terzaghi [4]. The consolidation theory will be followed in this project without dealing with the microscopic details of mechanisms of swelling. A disadvantage of this macroscopic approach is that it does not account for the water chemistry explicitly.

Chapter 3

In the second part, the exact geometry of the bentonite extrusion through fractures is described, the governing equations for bentonite swelling are established and their side-conditions chosen. Mass conservation and Darcy's laws [5] are assumed to be obeyed in the expanding bentonite region. Regarding the clay properties, the permeability and effective pressure have to be characterized as functions of the void ratio. A literature survey provided us with common analytical expressions for these quantities where a few parameters are to be chosen to fit the experimental measurements.

Chapters 4, 5 and 6

In the third part, which comprises of three chapters, the governing equations with the chosen boundary conditions are simulated with a time-dependent numerical algorithm based on a finite-element method. The theoretical model established in this work is validated by comparing the bentonite expansion with the analytical expression of the bentonite expansion derived by Terzaghi [6]. The comparison of the results shows an overall good agreement. Some numerical simulations are performed to study the sensitivity of the expansion to the permeability, effective pressure and other parameters.

1.4 CONCLUSION

Based on the theoretical model developed in this study and on some realistic values for the material properties, numerical calculations have been performed to

determine the radial expansion of a cylindrical volume of clay contacted with water. The numerical results show on one side the extent of the expansion and on the other its rate. As the extent uniquely depends on the initial and final or equilibrium states of the clay, the expansion rate depends heavily on the material properties, i.e. the permeability and the swelling coefficient of the clay. In all cases, the results show an expansion in less than 3000 years, which is relatively short as we know that the bentonite engineered barrier is assumed to last forever in performance assessment of geologic repositories. This study will certainly lead us to reconsider the performance assessment of engineered barriers, accounting now for the larger extent of the clay region. On one side the larger bentonite region could decrease the amount of radionuclides released to the environment but on another side, the integrity of the buffer material as an engineered barrier will become questionable because of the loss of bentonite.

1.5 FUTURE WORK

Several effects have been neglected in this study. Among them, two important ones are the initial unsaturated state of the clay and the shear stresses on the walls of the fracture. In order to include this last effect, our swelling model should be expanded to two dimensions. This could easily be done by adding two additional momentum conservation equations to our model. A two-dimensional analysis of the clay expansion through the fracture would give more realistic results as far as the expansion time and bentonite region extent are concerned. However, before going on further refinements of the present model, a comparison of our early numerical results with some experiments close to the case studied theoretically would prove useful to validate our model. Also, accurate measurements of the properties at the tip of the bentonite would be necessary.

1.6 REFERENCES FOR CHAPTER 1

[1] J.Ahn, P.L. Chambré, B. Light, D. Roberts, J. Verbeke, *Radioactive Transport in Disturbed Zone Between Engineered and Natural Barriers of Deep Geologic Disposal of High-Level Radioactive Wastes*, UCB-NE 4217, 1996.

[2] J.K. Mitchell, *Fundamentals of Soil Behaviour*, 2nd ed., Wiley, New York, 1993.

[3] P.F. Low, *Interparticle Forces in Clay Suspensions: Flocculation, Viscous Flow and Swelling*, Proc. 1989 Clay Min. Soc. Workshop on Rheology of Clay/Water Systems, 1992.

[4] K. Terzaghi, *The Influence of Elasticity and Permeability on the Swelling of Two-Phase Systems*, Colloid Chemistry, Vol. III, Chemical Catalog Co., New York, pp. 65-88, 1931.

[5] H. Darcy, *Détermination des lois d'écoulement de l'eau à travers le sable.* Les fontaines publiques de la ville de Dijon, pp. 590-594. Paris : Victor Dalmont, 1856.

[6] K. Terzaghi, Erdbaumechanik auf bodenphysikalischer Grundlage, Leipzig und Wien, F. Deuticke, 1925.

CHAPTER
TWO

BENTONITE SWELLING

In this chapter, we will do a survey of the literature to explain the mechanisms of bentonite swelling. Two different approaches have been considered by soil scientists. The first one is at a microscopic level and consists in studying the interactions of solid particles separated by a water layer containing cations. The main theories derived from this microscopic approach are the electrical double layer theory [1] and the hydration theory [2]. However, none of these theories reproduce satisfactorily the experimental swelling pressure. The second approach does not take these microscopic interactions into account but replaces this complexity by an empirical expression relating the effective stress to the void ratio. Our model will be based on the so-called consolidation theory [3].

2.1 BASIC STRUCTURAL UNIT

Silica and gibbsite are the two principal units composing montmorillonite, the major mineral in bentonite. These basic units are represented in Figure 2.1

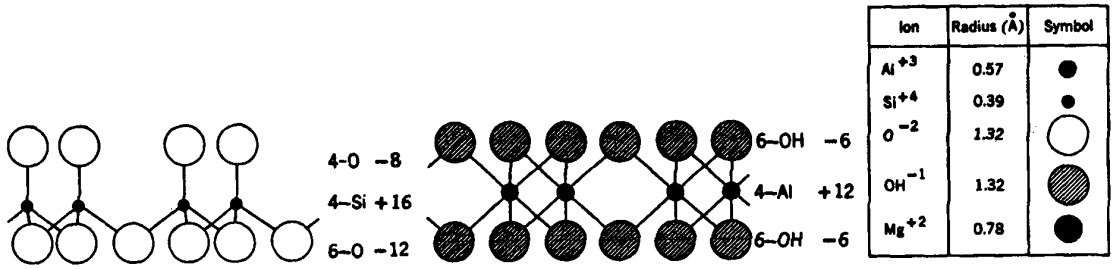

Figure 2.1 Basic units of silica (left) and gibbsite (right) [4].

The silicon-oxygen tetrahedron consists of four oxygens nestled around a silicon atom to form the unit. Combining the silicon-oxygen tetrahedrons gives the silica sheet shown in the left figure. The atoms are drawn to scale on the basis of the radii in units of angstroms given in the table. The number at the right of each unit gives the valence. Combining the aluminum-oxygen octahedrons gives gibbsite. From the valences shown in the figure, silica is not neutral, whereas gibbsite is.

Figure 2.2 shows the dimensions of the tetrahedra and octahedra sheets. Because both sheets have the same lattice constants (5.2 and 9.0 Å), oxygens or hydrogen peroxides on both sides of gibbsite can be shared by apical oxygens of silica.

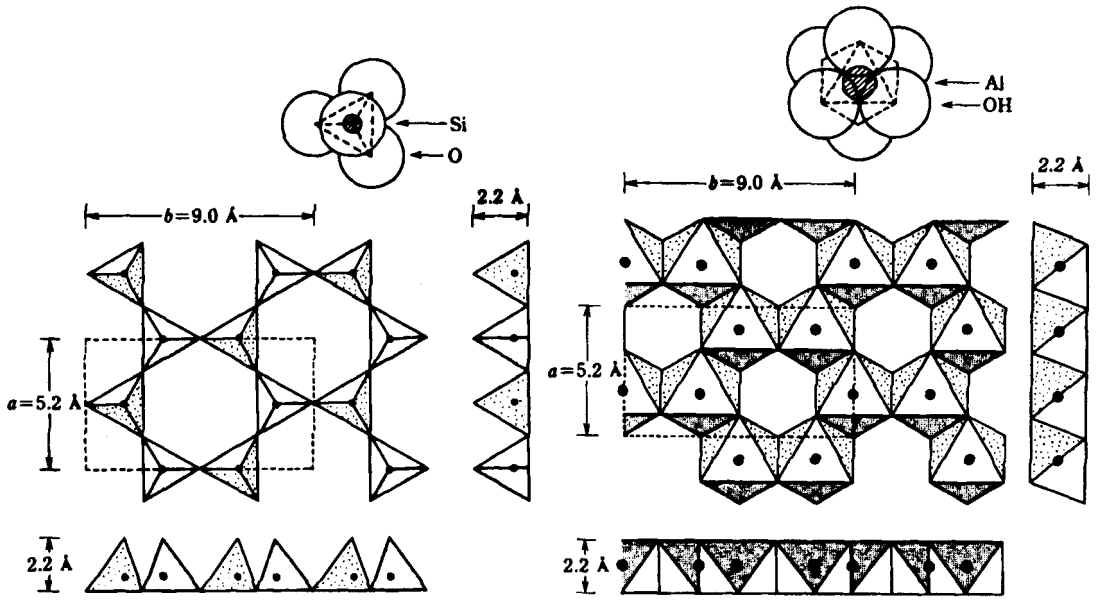

Figure 2.2 Two-dimensional views of silica and gibbsite.

Figure 2.3 shows the mineral pyrophyllite made of a gibbsite sandwiched between two silica sheets. Montmorillonite has a structure similar to pyrophyllite with the exception that there has been isomorphous substitution of one magnesium atom for every six aluminum atoms in the gibbsite sheet.

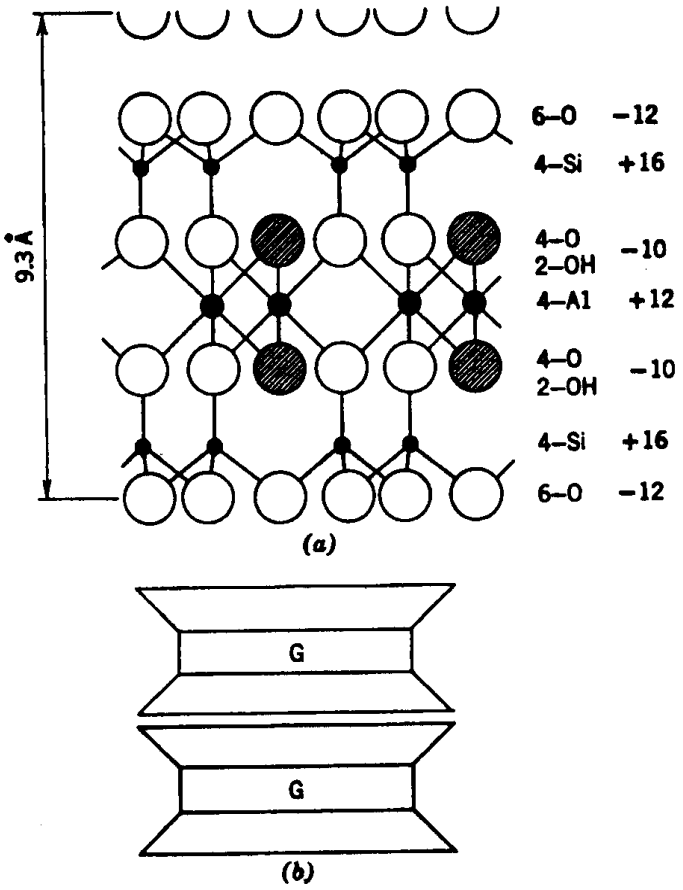

Figure 2.3 The structure of pyrophyllite. (a) Atomic structure. (b) Symbolic structure.

2.2 ELECTRICAL CHARGE ON A BENTONITE PARTICLE

With the dimensions shown in Figures 2.2 and 2.3, the specific surface and the surface area per unit charge deficiency of montmorillonite can be calculated as follows.

The surface area per unit is: 2(top and bottom)×5.2Å×9.0Å=93.6 $Å^2$

Volume per unit is: 93.6$Å^2$×9.3Å/2=435 $Å^3$

Weight per unit is: 435$Å^3$×$10^{-24}$$cm^3$/$Å^3$×2.76 g/$cm^3$=1200×$10^{-24}$ g

Specific charge is: (93.6$Å^2$×$10^{-20}$$m^2$/$Å^2$) /(1200×$10^{-24}$g)=780 m^2/g

Charge deficiency is: 1 per 6 cations in gibbsite

4 cations in the unit

Charge deficiency per unit is: 2/3

Surface area per unit charge deficiency is 93.6$Å^2$/(2/3)=140 $Å^2$

The computed values are close to the experimental values of 800 m^2/g and 133 $Å^2$[4], respectively. Because of this large specific surface (compare 10 to 20 m^2/g for kaolinite), influence of electrical forces, which are directly related to the surface area, on the behaviour of the particle is of primary importance, and thus the particle is characterized as colloid.

2.3 ELECTRICAL DOUBLE LAYER: GENERAL OBSERVATION

Let us now consider the nature of a particle in water. A typical particle of montmorillonite, which is one of the smallest minerals in clay, has dimensions of 1000Å×1000Å(surface area)×10Å(thickness) [4]. Considering both top and bottom surfaces, the particle has 2×10^6 $Å^2$ of surface area. The total number of charge deficiency on the montmorillonite particle is calculated as $2\times10^6Å^2/140Å^2$=14,000. Thus the montmorillonite particle would carry 14,000 sodium ions to compensate the charge deficiency on the particle.

If the individual particles are now dropped into water, both mineral surface and the exchangeable ions (sodium) pick up water, i.e., hydrate. Upon hydration, the sodium ion grows about sevenfold, as illustrated in Figure 2.4 As the scaled drawings indicate, the hydrated sodium ions are too large to fit into a monoionic layer on the particles. Actually, the exchangeable ions with their shells of water move away from the mineral surfaces to positions of equilibrium. The ions are attracted to the mineral surface to satisfy the negative charge existing within the surface. They also desire to move away from each other because of their thermal energies. The actual positions they occupy are compromises between these two types of forces.

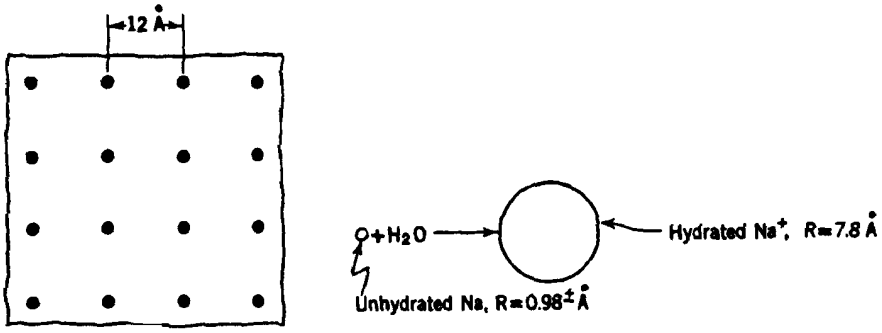

Figure 2.4 Particle surface with exchangeable ions. Surface of dry montmorillonite.

Figure 2.5 shows the distributions of ions around the surface and a plot of electrical potential versus distance from the surface. The water in the double layer is under an attractive force to the particle since this water is attracted to the exchangeable ions which are in turn attracted to the soil surface (β-planes). Water is also attracted to the mineral surface by other forces such as the force between the polar water and the electrical

charges on the particle surface, hydrogen bonding, and van der Waals forces. The structured region of the double layer is commonly considered to include α-planes and β-planes; the thickness of this ordered region is believed to extend to about 5 Å (about two water molecules thick). If we assume that the thickness of the strongly attracted water region is 5 Å, $780 m^2/g \times 1g \times 5Å \times 10^6 g/m^3 = 0.4$ g of water is bound to 1 g of the solid phase.

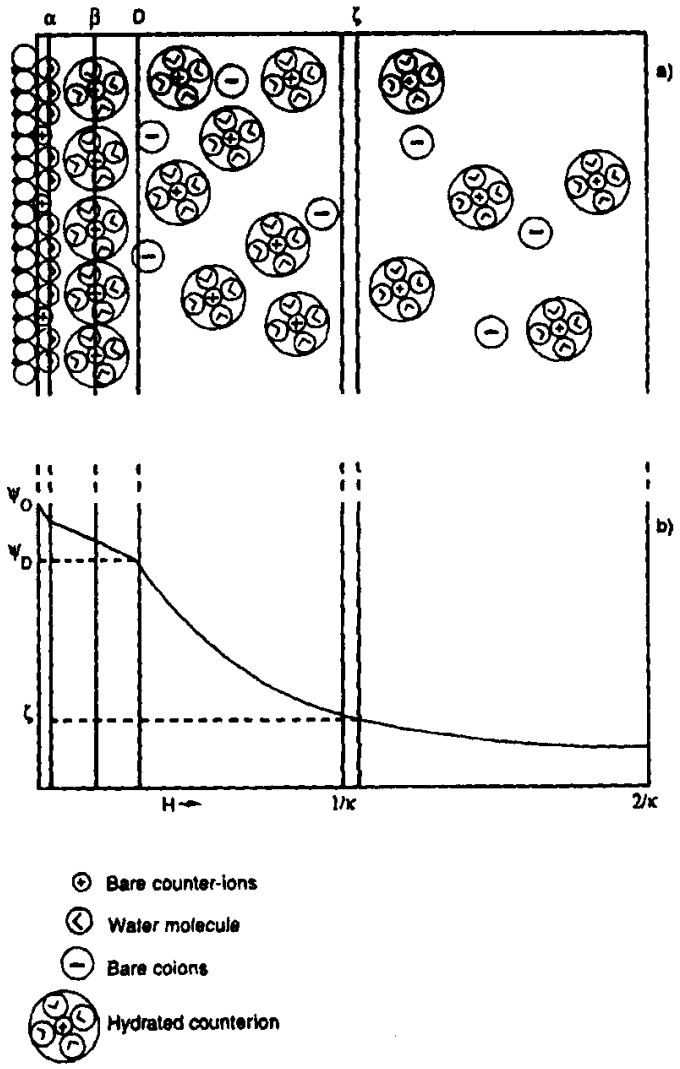

Figure 2.5 (a) A hypothetical model for a multilayer configuration of clay-water interphase. (b) Decay of the surface potential in the interphase region (clay surface is represented by the basal oxygens and the tetrahedral cations.) [2].

The α-plane (or inner Helmholtz plane) is comprised mainly of oriented water dipoles on the particle surfaces. The β-plane represents the first plane of hydrated counterions next to the surface. The D-plane (or outer- Helmholtz plane) marks the

beginning of the diffuse double layer. The $(1/\kappa)$ plane is most likely somewhere in the diffuse layer where the potential drops to 1/e of the surface potential. The ζ-plane is the slip (shear) plane delineating the section of the double layer that moves with the particle. This plane may be close to the $(1/\kappa)$ plane. Distribution of counterions in α-planes and β-planes is expected to be discrete in the form of an array. Potential is assumed to drop linearly from the particle surface to α- β-planes and then decay exponentially within the diffuse layer.

If we take two montmorillonite particles which are far apart and then bring them toward each other, they will reach an interparticle spacing at which they begin to exert forces on each other. Since each particle carries a net negative charge, the two particles repel each other because of the Coulombic electrical force between like charges. We denote this force as *R'*. Since the negative charge on a particle is balanced by the cations in the double layer, the two advancing particles begin to repel each other when their double layers come into contact with one another. The repulsive force between the adjacent particles for any given spacing is therefore directly related to the sizes of the double layers on the two particles.

In addition to a repulsive force between the approaching particles, there is also a component of attractive force *A'* between two particles. This attractive force is the Van der Waals' force, acting between all adjacent pieces of matter.

Net energy of interaction can be estimated, based on the preceding argument [1]. The plot of the net energy versus the interparticle distance may take many forms depending on the double layer parameters, such as the distance parameter κ, the surface potential Ψ_0, the cation concentration, and so on. The main features of the net potential curve are schematically illustrated in Figure 2.6

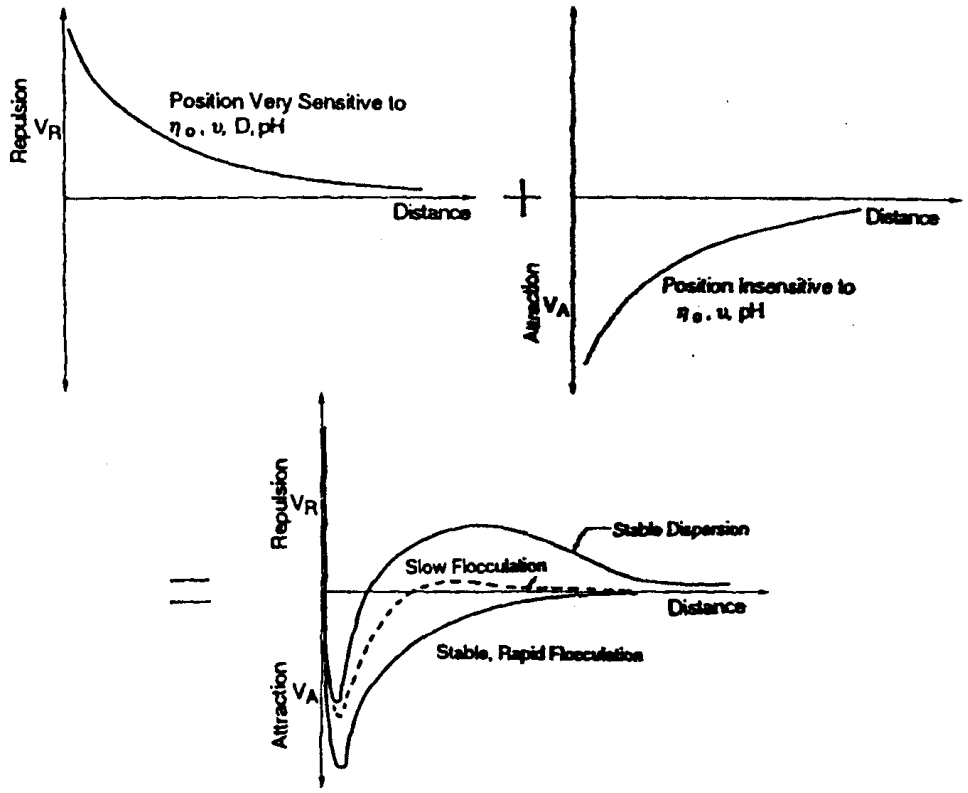

Figure 2.6 Energies of repulsion, attraction, and net curves of interaction for parallel plates.

Although the model based on the double layer theory is successful in explaining many important features of clay minerals, serious shortcomings are also reported. Low [2] reviewed his experimental data collected during the last thirty years on the swelling of a large number of Na-montmorillonite, and found a great discrepancy between the measured swelling pressure and the pressure calculated based on the view described above. He claimed that about 2% of counterions dissociate into the diffuse layer; the rest remaining in the Stern layer. Low proposed in his hydration theory an empirically derived equation expressing the relationship between the swelling pressure π (in atmospheres) and the water/clay mass ratio w in the system

$$p + 1 = B \exp\left(\frac{a}{w}\right), \qquad (2.1)$$

where B and α are empirical constants to be determined by experiments.

Although the hydration theory can reproduce experimental measurements very well, it lacks mechanistic basis. Two empirical constants represent all the complexity.

In summary, a theory that consistently explains observations with various clay minerals has not yet been developed.

2.4 TERZAGHI'S DEFINITION OF THE EFFECTIVE STRESS IN A SATURATED MEDIUM

In this section, the concept of effective stress [3] will be explained using a simple example. We will consider a water-saturated layer of clay of thickness d lying on an impermeable layer. The water level is h_0 above the clay surface. Several pressure tubes are standing in the clay layer at different depth d-z. At times $t<0$, a pressure p_1 is uniformly applied on the clay. The clay is in hydraulic equilibrium with the water above. According to this assumption, the water in the different pressure tubes reaches the same level h_0.

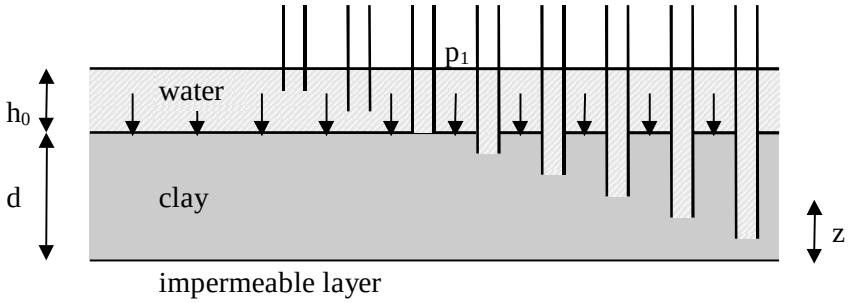

Figure 2.7 Water pressure in the clay for times $t<0$.

The water pressure at the bottom of each tube is given by

$$p_w = r_w g(d - z + h_0) \tag{2.2}$$

where d-z+h_0 denotes the water level in the pressure tubes.

Since this water pressure p_w acts in every direction in the water and solid phases with the same intensity, it does not have a measurable influence on the void ratio or mechanical properties of the soil. It is termed the neutral normal stress. The total normal stress at a given depth d-z is

$$s = r_w g h_0 + rg(d - z) + p_1, \tag{2.3}$$

where ρ is the density of the saturated clay [kg/m^3].

The total normal stress σ comprises of two parts: the neutral normal stress p_w, which acts in the water as well as in the solid phase and the effective stress

$$s' = s - p_w, \tag{2.4}$$

which represents the excess over the neutral normal stress p_w and has its seat exclusively on the solid phase of the soil.

At the time t=0, the pressure p_1 is uniformly removed from the clay.

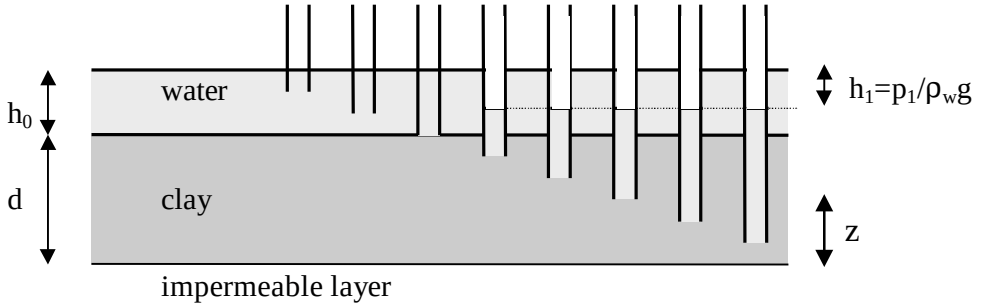

Figure 2.8 Water pressure in the clay at the time t=0.

The total normal stress σ and the neutral normal stress p_w decrease by the pressure p_1 and the water in the clay is not in hydraulic equilibrium with the free water above anymore. However, free water is not absorbed instantaneously because of the low permeability of the clay. The solid microstructure remains thus the same, i.e., the void ratio is still equal to the initial one. By the definition (2.4), the effective stress σ' remains the same as before.

As the time goes on, the water is slowly absorbed by the clay because of the water pressure difference at the free water/clay interface. The neutral normal stress p_w increases and the void ratio rises as water flows in. Since the water pressure above the clay still has to be balanced by the total normal stress σ, the effective stress σ' decreases according to (2.4).

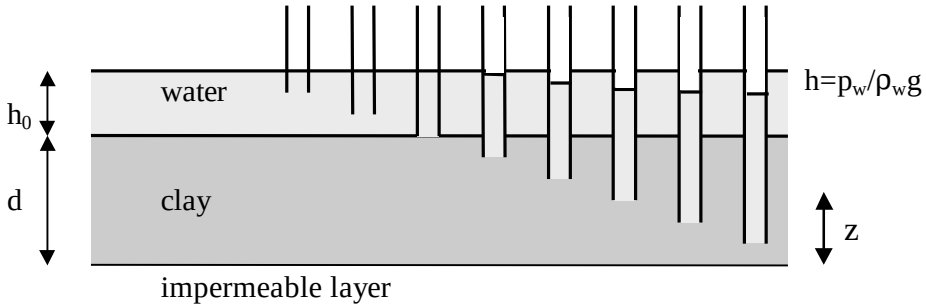

Figure 2.9 Water pressure at some later time $0<t<\infty$.

The void ratio increases until the neutral normal stress p_w increase is compensated for by an equal decrease in the effective stress σ'.

From the two last pictures, we can conclude that the change in effective stress σ' is accompanied by a change in the clay microstructure or similarly void ratio, what influences strongly the mechanical properties of the soil, whereas the change in neutral normal stress p_w has no effect on them.

When the time t goes to infinity, more water flows into the clay and eventually, the neutral normal stress p_w increases to its initial value and a new hydraulic equilibrium

with the free water is established. The void ratio rises to the point where the effective stress σ' has decreased by the pressure p_1.

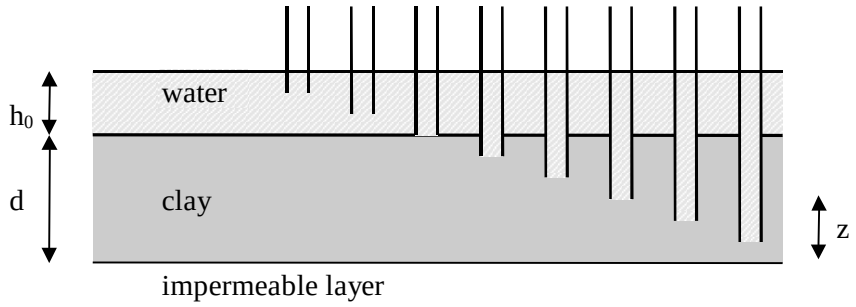

Figure 2.10 Stationary water pressure for $t \to ¥$.

At any time during this swelling process the total stress σ is the sum of the effective stress σ' and the neutral normal stress p_w:

$$s = s' + p_w. \tag{2.5}$$

2.5 MICROSCOPIC DEFINITION OF THE EFFECTIVE STRESS IN A PARTIALLY SATURATED MEDIUM

Although the relationship (2.4) was the original definition of the effective stress by Terzaghi, we will rewrite it in the more general case of a partially saturated medium by considering the acting forces at a microscopic scale. In any cross-section of the clay, the total normal force exerted on the cross-section is equal to the sum of four components: the forces carried by the mineral, the air phase, the water phase, and the difference between the electrical repulsive forces *R'* and attractive forces *A'*. Dividing by the area of the cross-section, we get the following relationship

$$s = s_m a_m + p_a a_a + p_w a_w + R - A \tag{2.6}$$

where σ is the total normal stress [Pa],
σ_m is the stress where contact is mineral-mineral [Pa],
p_a is the air pressure [Pa],
p_w is the water pressure [Pa],
R and *A* are the electrical repulsive and attractive forces divided by the area of the cross-section,
a_m, a_a and a_w are the fractions of the cross-section occupied by the mineral, air and water respectively.

The contact stress σ_m in montmorillonite can be zero, due to its structure. In a partially saturated medium, $a_m \approx 0$ and $a_a + a_w \approx 1$. Thus, (2.6) can be rewritten as

$$s = p_a(1-a_w) + p_w a_w + R - A \qquad (2.7)$$

In the general case of a partially saturated medium, the repulsive stresses R minus attractive stresses A represent the swelling pressure π. The expression (2.7) becomes then

$$s = p_a(1-a_w) + p_w a_w + p\ . \qquad (2.8)$$

With Bishop's parameter χ, which is to be determined by experiments and has a strong non-linear relation to the degree of saturation S, (2.8) can be written as

$$s = p_w c + p \quad \text{with } 0 \le \chi \le 1 \qquad (2.9)$$

where χ becomes unity when the medium is saturated *(S=1)*.

The effective stress σ' in an unsaturated medium is defined by the relation [4]

$$s' = s - p_w c\ , \qquad (2.10)$$

which becomes identical to (2.5) in a saturated medium, $\chi=1$. This shows the agreement with Terzaghi's theory. The total normal stress acts over the entire area of the cross-section (including solid skeleton and voids), and the pore water pressure p_w acts over the total area minus the mineral contact area. The effective stress is the force carried by the skeleton divided by the total area of the cross section. Comparing (2.9) and (2.10), we obtain

$$s' = p\ . \qquad (2.11)$$

We now make an assumption that is reasonable in a rock fracture that the total stress σ at any point in the system does not change in time. Then, the changes in effective stress and pore water pressure are related by, from (2.10),

$$\frac{ds'}{dp_w} = -c' \ \text{ with } \ c' = c + p_w \frac{dc}{dp_w}\ . \qquad (2.12)$$

2.6 REFERENCES FOR CHAPTER 2

[1] J.K. Mitchell, *Fundamentals of Soil Behaviour*, 2nd ed., Wiley, New York, 1993.

[2] P.F. Low, *Interparticle Forces in Clay Suspensions: Flocculation, Viscous Flow and Swelling*, Proc. 1989 Clay Min. Soc. Workshop on Rheology of Clay/Water Systems, 1992.

[3] K. Terzaghi, *The Influence of Elasticity and Permeability on the Swelling of Two-Phase Systems*, Colloid Chemistry, Vol. III, Chemical Catalog Co., New York, pp. 65-88, 1931.

[4] T.W. Lambe, R.V. Whitman, *Soil Mechanics*, Wiley, New York, 1969.

CHAPTER
THREE

GOVERNING EQUATIONS

In this chapter, the governing equations for the bentonite expansion problem are established based on Terzaghi's consolidation theory [1], a mass conservation law and Darcy's law [2]. They are subject to some realistic assumptions mentioned in the text. Analytical expressions for the permeability and coefficient of swelling are proposed. Initial and boundary conditions are then discussed.

3.1 MASS CONSERVATION EQUATION

The fundamental equation of transient groundwater motion is an equation of mass conservation. For a flow region which deforms with time the mass conservation equation can be written in an integral form as

$$\frac{D}{Dt}\int_{V(t)} \rho_w q\, dV = -\int_{\Gamma(t)} \rho_w \vec{q}\vec{n}\, d\Gamma, \qquad (3.1)$$

where $\frac{D\bullet}{Dt} = \frac{\partial \bullet}{\partial t} + v\frac{\partial \bullet}{\partial x}$ stands for the material derivative,

$V(t)$ is an infinitesimally small volume element of boundary $\Gamma(t)$,

v is the average velocity of the volume element $V(t)$,

ρ_w is the water density [kg/m^3],

q is the volumetric moisture content defined as the ratio of the water volume to the total volume [-],

$\vec{q}$ is the vector flux density of water relative to the solid grains [m/s],

$\vec{n}$ is the outward vector normal to the surface element $\Gamma(t)$.

This mass conservation law expresses that the mass of water contained in the volume element $V(t)$ changes by the mass of water flowing in and out of this volume through its surface $\Gamma(t)$. Since we are concerned with a deformable porous medium, the volume element $V(t)$ is chosen in such a way that it contains a constant solid volume V_s and a variable void volume $V_v(t)$. The expansion by water absorption of the volume element $V(t)$ is expressed by the spatial partial derivative in the material derivative. However, in order to simplify the equations, we will introduce the approximation that this term can be neglected.

Using Gauss' theorem in the right-hand side of (3.1), this expression can be rewritten as

$$\frac{\partial}{\partial t}\int_{V(t)} \rho_w q\, dV = -\int_{V(t)} \nabla\left(\rho_w \vec{q}\right) dV \,. \tag{3.2}$$

If the volume element *V(t)* is appropriately small so that ρ_w, q and $\nabla\vec{q}$ can be treated as average values over *V(t)*, then (3.2) becomes

$$\frac{\partial}{\partial t}\left(\rho_w q V\right) = -\nabla\left(\rho_w \vec{q}\right) V \,. \tag{3.3}$$

The flux density of water $\vec{q}$ can be related to the hydraulic head h using Darcy's law [2], which reads

$$\vec{q} = -\frac{k\rho_w g}{\mu}\nabla h \,, \tag{3.4}$$

where μ is the coefficient of viscosity of water [kg/m/sec],

h is the hydraulic head, which can be expressed as $z + \dfrac{p_w}{\rho_w g}$ [m], and (3.5)

z is the elevation [m].

Since we are interested in horizontal fractures in the host rock, $\nabla z = 0$. If ρ_w, *V(t)*, the porosity n and the degree of saturation S are assumed to be functions of p_w only, which is justified from empirical considerations, then since $q = nS$, substitution of (3.4) into (3.3) leads to

$$M_c \frac{\partial p_w}{\partial t} = \nabla\left(\frac{\rho_w k}{\mu}\nabla p_w\right) V \,. \tag{3.6}$$

where $M_c = \dfrac{d}{dp_w}\left(\rho_w nSV\right)$ is the fluid mass capacity, (3.7)

n is the porosity defined as the ratio of the void volume to the total volume,
S is the degree of saturation defined as the ratio of the volume of water to the void volume.

The fluid mass capacity represents the mass of water which is absorbed by the volume element *V(t)* due to a unit change in the average value of p_w over *V(t)*. Since $nV = V_v = eV_s$, the fluid mass capacity (3.7) can be rewritten as

$$M_c = nSV\frac{d\rho_w}{dp_w} + \rho_w SV_s\frac{de}{dp_w} + \rho_w eV_s\frac{dS}{dp_w} \,. \tag{3.8}$$

The three terms on the right denote three distinct physical phenomena. The first term expresses the ability of water to expand due to changes in hydrostatic pressure, the second represents the deformability of the soil skeleton, and the last represents the

desaturation of the pores. We will assume here that the water is incompressible and the first term disappears. With (2.12), the second term of equation (3.8) reads now

$$r_w SV_s \frac{de}{dp_w} = r_w SV_s \frac{de}{ds'} \frac{ds'}{dp_w} = -r_w SV_s c' \frac{de}{ds'} \tag{3.9}$$

In soil mechanics literature it is customary to express stress-strain relationships of soils by plotting e versus σ_v', where σ_v' is the effective vertical stress applied by a piston in a uniaxial test. Figure **3.1** shows an example of this relationship. Initially, the specimen has an initial void ratio of 3.5 and is at the point *a*. As the specimen is compressed, it follows the compression curve to the point *b* where it rebounds to the point *c* after removal of the load. It is then recompressed to the point *d*, and so on. This figure shows the compression curve *abdf*, three rebound curves *bc*, *de*, *fg* and two recompression curves *cb* and *ed*. As we can observe on Figure **3.1**, the compression and swelling curves depend thus on the initial compression state of the clay. For each of the swelling curves *bc*, *de* and *fg*, analysis of a large number of uniaxial test data indicates that a plot of e versus log σ_v' is approximately a straight line on most of the void ratio range. The slope of the best-fitting straight line is called the 'swelling index'C_s, obtained as

$$C_s = -\frac{de}{d\log_{10} s'_v} = 2.303 s'_v a_v \tag{3.10}$$

where $a_v(e) = -\frac{de}{ds'_v}$ is the coefficient of swelling. (3.11)

Under the condition that the strains in the intermediate and minor principal stress directions are negligible and all possible strains occur in the major principal stress direction, the situation is very close to the uniaxial loading experiments conducted in the laboratory. In this case, the effective stress σ' can be replaced by the effective vertical stress σ_v'.

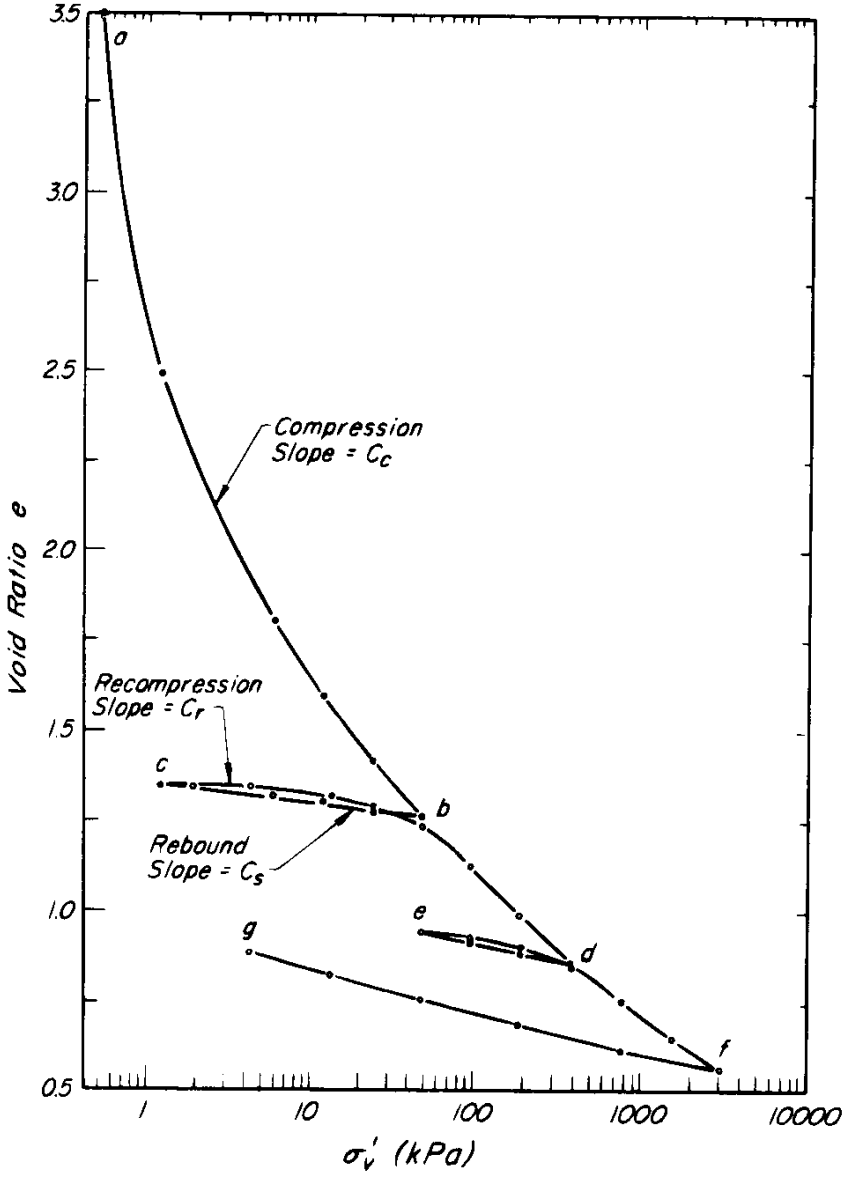

Figure 3.1 Relation between end-of-primary void ratio and log effective vertical stress σ_v' [3].

With (3.11), we can rewrite equation (3.9) as following:

$$r_w S V_s \frac{de}{dp_w} = r_w S V_s c' a_v . \qquad (3.12)$$

Substituting (3.12) into (3.8) gives the final expression for M_c as

$$M_c = r_w V_s \left(S a_v c' + e \frac{dS}{dp_w} \right). \tag{3.13}$$

Using (3.13), (3.6) can be rewritten as

$$\frac{1}{1+e} \left(S a_v c' + e \frac{dS}{dp_w} \right) \frac{\partial p_w}{\partial t} = \nabla \left(\frac{k}{m} \nabla p_w \right) \tag{3.14}$$

by noting that $V_s = \dfrac{V}{1+e}$. (3.15)

Equation (3.14) is the fundamental equation which describes the behaviour of a deformable medium with incompressible fluid. The permeability*k* is a function of *S*, which is a function of p_w. The void ratio *e* is also a function of p_w.

3.2 BENTONITE SATURATED WITH WATER

If we assume that bentonite is saturated with water, i.e. *S*=1, then (3.14) reduces to

$$\frac{1}{1+e} \frac{\partial e}{\partial t} = \nabla \left(\frac{k}{m} \nabla p_w \right) \tag{3.16}$$

By the chain rule of derivative and using equations (2.12) and (3.11), we get

$$\nabla p_w = \frac{dp_w}{ds'} \frac{ds'}{de} \nabla e = (-1) \left(-\frac{1}{a_v} \right) \nabla e = \frac{1}{a_v} \nabla e \tag{3.17}$$

In a cylindrical coordinate system, assuming axisymmetry and no dependence on *z*, this equation rewrites

$$\frac{1}{1+e} \frac{\partial e}{\partial t} = \frac{1}{r} \frac{\partial}{\partial r} \left(\frac{k(e)}{m a_v(e)} r \frac{\partial e}{\partial r} \right). \tag{3.18}$$

For the *e*-dependencies of the permeability and the coefficient of swelling, we need measurements for a particular bentonite of interest. However, from many previous experiments, such as illustrated in Figure **3.1** for a_v and in Figure **3.2** for *k*, we can express the *e*-dependencies as follows.

For the compressibility coefficient, from (3.10), a_v is expressed as

$$a_v = \frac{C_s}{2.303 s'}. \tag{3.19}$$

Subsituting a_v into (3.11) the effective stress can be obtained as

$$s' = s'_0 \exp\left(-\frac{2.303}{C_s}\left(e - e_0^s\right)\right) \tag{3.20}$$

where s'_0 and e_0^s represent an arbitrarily chosen point.

With (3.20), (3.19) can be modified as

$$a_v = \frac{C_s}{2.303\, s'_0} \exp\left(\frac{2.303}{C_s}\left(e - e_0^s\right)\right). \tag{3.21}$$

For the permeability, as is shown in Figure **3.2**, experimental data show a linear relationship between e and log K, where K is the hydraulic conductivity defined as $K = k\frac{r_w g}{m}$. We can therefore represent k as an exponential function of e:

$$k = k_0 \exp\left(\frac{2.303}{C_k}\left(e - e_0^k\right)\right) \tag{3.22}$$

where C_k is the best fitting straight line for the relationship of e versus $log\ k$,
k_0 and e_0^k represent an arbitrarily chosen point.

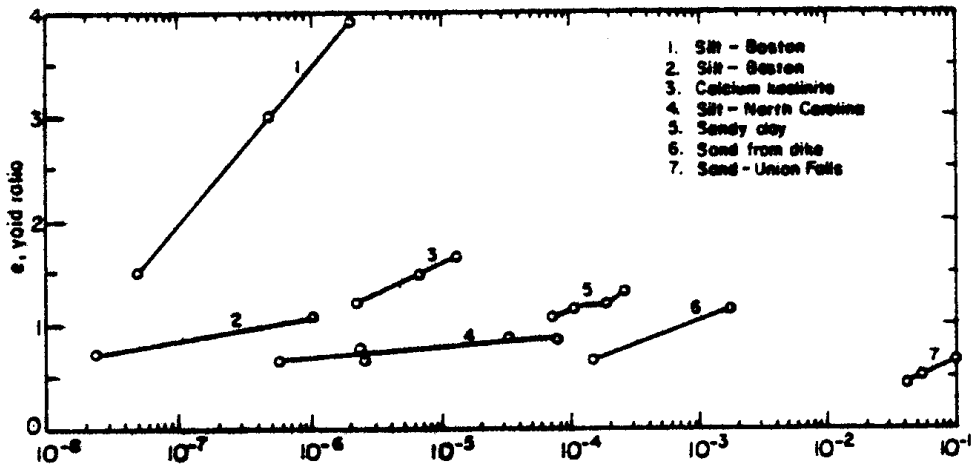

Figure 3.2 Relation between void ratio and log K [4].

Equation (3.22) is only one way of representing the dependence of permeability on effective stress. As far as numerical modeling is concerned, one could equally well use any other convenient experimental relationship or simply tabulate k as a function of effective stress.

With the two last relationships (3.21) for a_v and (3.22) for k, we obtain the final expression for the governing equation

$$\frac{1}{1+e}\frac{\partial e}{\partial t} = \frac{C}{r}\frac{\partial}{\partial r}\left(r \exp(Ge)\frac{\partial e}{\partial r}\right) \tag{3.23}$$

where $$G = 2.303\left(\frac{1}{C_k} - \frac{1}{C_s}\right), \tag{3.24}$$

$$C = \frac{2.303 s_0' k_0}{m C_s} \exp\left[2.303\left(\frac{e_0^s}{C_s} - \frac{e_0^k}{C_k}\right)\right]. \tag{3.25}$$

3.3 BENTONITE EXPANSION

We pointed out earlier that the bentonite was expanding. Hence, the domain on which equation (3.23) has to be solved is increasing in size. This expansion effect is not taken into account by the formulation (3.23) because the spatial derivative in the material derivative has been neglected. Thus, we need a second equation to express this expansion as a function of time. We will derive here the expression for the position of the moving boundary as a function of time.

Since the bentonite expansion largely depends on its volume and on the surface area of the interface bentonite/free water, we have to fix the geometry of the system to derive the expansion. The geometry is defined as shown in Figure **3.3** We consider a cylindrical volume of bentonite of radius *R(t)* expanding in a fracture of width *L*. The bentonite is surrounded by free water in such a way that water absorption occurs only at the location of the tip *R(t)* of the bentonite. We also assume axisymmetry and no *z*-dependency in the fracture.

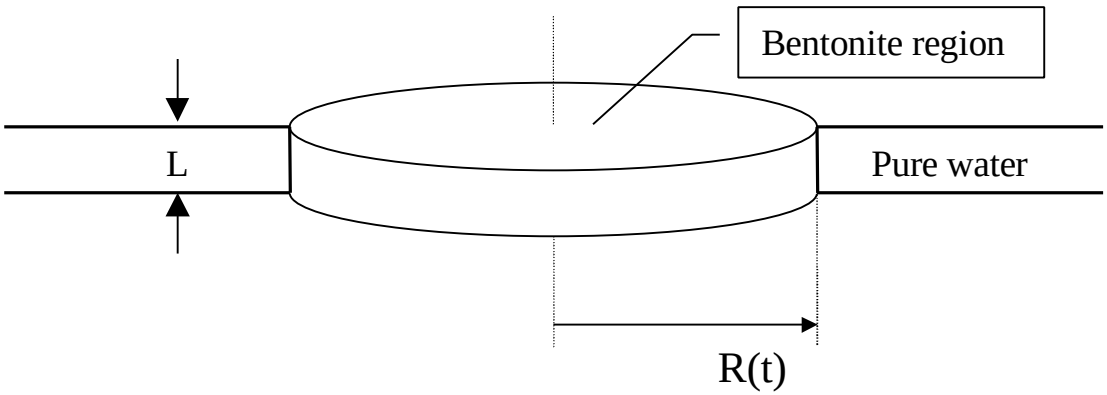

Figure 3.3 Geometrical definition of the bentonite volume expanding in the fracture.

The mass conservation equation (3.1) is rewritten for the whole volume of bentonite between *r=0* and *r=R(t)*:

$$\frac{d}{dt}\left(\rho_w V_{water}\right) = -A \rho_w \vec{q}\vec{n}\big|_{r=R(t)}, \tag{3.26}$$

where $A = 2pR(t)L$ is the surface area of the bentonite in contact with water at the interface bentonite/free water. This mass conservation law expresses that the mass of water contained in the whole volume of bentonite changes by the mass of water flowing into this volume through its surface in contact with free water.

The total volume of bentonite is the sum of the air, water and solid phase volumes, the volume of water can thus be rewritten as

$$V_{water}(t) = V_{total}(t) - V_{solid} - V_{air}(t) = pR^2(t)L - V_{solid} - V_{air}(t) \qquad (3.27)$$

Assuming that the medium is saturated, i.e. $V_{air}(t) = 0$, and that the water is incompressible, equation (3.26) reads now

$$\frac{dR(t)}{dt} = -\vec{q}\vec{n}\Big|_{r=R(t)}. \qquad (3.28)$$

Introducing Darcy's law (3.4) and using (3.5), we obtain

$$\frac{dR(t)}{dt} = -\frac{k}{m}\frac{\partial p_w}{\partial r}\Big|_{r=R(t)}. \qquad (3.29)$$

This fundamental equation describes the expansion of a cylindrical volume of a saturated medium contacted with water. The permeability k is a function of p_w.

Using (3.17), (3.21) and (3.22), the equation (3.29) can be rewritten as

$$\frac{dR(t)}{dt} = -C\exp(Ge)\frac{\partial e}{\partial r}\Big|_{r=R(t)} \qquad (3.30)$$

where C and G are given by (3.24) and (3.25).

3.4 INITIAL AND BOUNDARY CONDITIONS

The void ratio $e(r,t)$ in equation (3.23) has to be solved on the domain $0 \le r \le R(t)$ where $R(t)$ is given by equation (3.30). We still need some appropriate initial and boundary conditions to quantitatively estimate the volume expansion of the water-saturated bentonite as a function of time t and position r.

At the time t=0, the properties of the bentonite are homogeneous. Hence, the void ratio is uniformly equal to e_0 throughout the bentonite:

$$e(r,0) = e_0 \text{ for } 0 \le r \le R(0). \qquad (3.31)$$

At the location r=0, there is no water flow by symmetry. Using Darcy's law (3.4) with (3.5), we obtain

$$\vec{q}(0,t) = -\frac{k r_w g}{m} \left.\frac{\partial e}{\partial r}\right|_{r=0} = 0 \text{ or } \left.\frac{\partial e}{\partial r}\right|_{r=0} = 0 \text{ for } t>0. \qquad (3.32)$$

The last boundary condition is at the tip $r=R(t)$. At this location, the bentonite is always in equilibrium with the free water. Since the stress p_w in the free water is the same as the total stress σ in the bentonite, using (2.10), the void ratio e_{limit} at the tip should be such that $\sigma'(e_{limit}) = p_w - p_w^{tip}$. We will make the assumption that the right-hand side, i.e. the difference between the water pressure in the fracture p_w and the water pressure at the tip p_w^{tip}, is a known positive constant. Since there is only one curve $\sigma'(e)$, the void ratio at the tip could be determined by equating $\sigma'(e_{limit})$ to this constant. Figure **3.4** represents the relationship (2.10) with the assumption made.

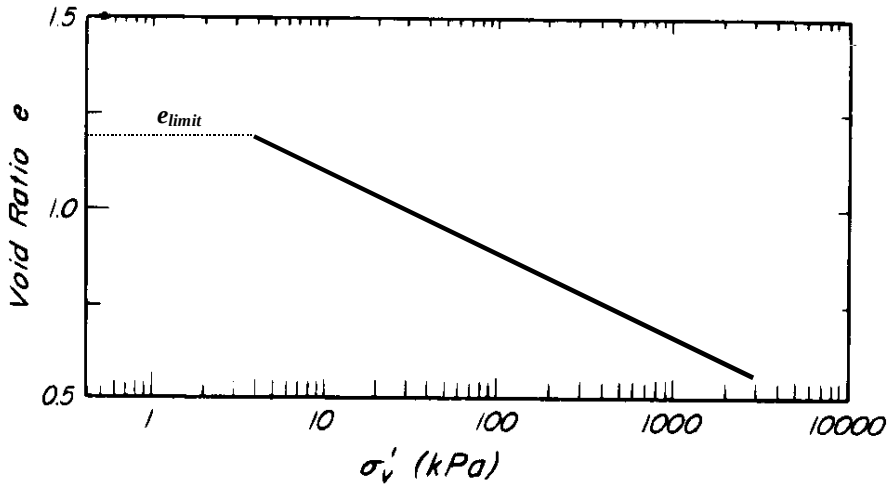

Figure 3.4 Modified relation between void ratio and log s'.

This assumption and new relationship should be validated by measurements of the effective pressure for high void ratios and by experimental determination of e_{limit}. The equilibrium boundary condition $\sigma'(e_{limit}) = p_w - p_w^{tip}$ at the tip can be written as

$$e(R(t),t) = e_{\text{limit}} \text{ for } t>0. \qquad (3.34)$$

3.5 PREDICTION OF THE FINAL TIP POSITION

At the time t=0, the void ratio $e(r,0)$ is uniformly equal to e_0 throughout the bentonite, thus the ratio of the two-phase mixture volume to the solid volume is given by

$$\frac{V_{total}(0)}{V_{solid}(0)} = 1 + e_0 . \tag{3.35}$$

Since the governing equation is of the diffusion-type, when the time approaches infinity, the void ratio throughout the bentonite tends uniformly to the void ratio at the tip e_{limit}. The ratio above becomes then

$$\lim_{t\to\infty} \frac{V_{total}(t)}{V_{solid}(t)} = 1 + e_{\text{limit}} . \tag{3.36}$$

With the assumption of incompressibility for the solid phase, the solid mass conservation implies the solid volume conservation and $V_{solid}(0) = \lim_{t\to\infty} V_{solid}(t)$. Dividing equation (3.36) by (3.35), we obtain

$$\lim_{t\to\infty} \frac{V_{total}(t)}{V_{total}(0)} = \frac{1 + e_{\text{limit}}}{1 + e_0} . \tag{3.37}$$

At all times, the total volume is given by

$$V_{total}(t) = LpR^2(t) . \tag{3.38}$$

Substituting (3.38) in (3.37), the radius of the bentonite when the time t approaches infinity becomes

$$\lim_{t\to\infty} R(t) = R(0)\sqrt{\frac{1 + e_{\text{limit}}}{1 + e_0}} . \tag{3.39}$$

3.6 REFERENCES FOR CHAPTER 3

[1] K. Terzaghi, Erdbaumechanik auf bodenphysikalischer Grundlage, Leipzig und Wien, F. Deuticke, 1925.

[2] H. Darcy, *Détermination des lois d'écoulement de l'eau à travers le sable.* Les fontaines publiques de la ville de Dijon, pp. 590-594. Paris : Victor Dalmont, 1856.

[3] K. Terzaghi, R.B. Peck, G. Mesri, *Soil Mechanics in Engineering Practice,* 3rd ed., Wiley-Interscience, 1996.

[4] T.W. Lambe, R.V. Whitman, *Soil Mechanics,* Wiley, New York, 1969.

CHAPTER
FOUR

SOLUTION FOR THE GOVERNING EQUATIONS

In this chapter, we establish a numerical scheme to simulate our governing equations. The basic algorithm is based on a fully implicit Galerkin/Finite Element technique on deforming elements combined with a predictor-corrector scheme. By combination of the predictor and the corrector, the temporal accuracy can be controlled by automatic time step modification.

4.1 PROBLEM STATEMENT

The problem of the bentonite expansion in a planar fracture by water absorption can be summarized in the following form, where *e(r,t)* and *R(t)* are the unknowns to be solved for:

Governing equations:

$$\frac{C}{r}\frac{\partial}{\partial r}\left[r\exp(Ge)\frac{\partial e}{\partial r}\right]=\frac{1}{1+e}\frac{\partial e}{\partial t}\ \text{ on } 0\le r\le R(t) \text{ for } t>0, \tag{4.1}$$

$$\frac{dR(t)}{dt}=C\exp(Ge)\left.\frac{\partial e}{\partial r}\right|_{r=R(t)}\ \text{ for } t>0, \tag{4.2}$$

where $\begin{cases} G=2.303\left(\dfrac{1}{C_k}-\dfrac{1}{C_s}\right) \\ C=\dfrac{2.303 s_0' k_0}{m C_s}\exp\left[2.303\left(\dfrac{e_0^s}{C_s}-\dfrac{e_0^k}{C_k}\right)\right] \end{cases}$.

Initial conditions:

$$e(r,0)=e_0\ \text{ on } 0\le r\le R(0), \tag{4.3}$$

$$R(0)=R_0. \tag{4.4}$$

Boundary conditions:

$$\frac{\partial e}{\partial r}=0\ \text{ for } r=0,\ t>0, \tag{4.5}$$

$$e=e_{\text{limit}}\ \text{ for } r=R(t),\ t>0. \tag{4.6}$$

No analytical solution exists for this problem. However, by introducing some approximations, an analytical solution can be found and will be proposed in the next chapter. Equation (4.1) is non-linear and contains an advective-type term $e\vec{\nabla}e$, two features which make the problem difficult to solve numerically.

4.2 SPATIAL DISCRETIZATION VIA GALERKIN METHOD

The finite element spatial discretization of equation (4.1), so-called semi-discretization in space, is performed via the Galerkin method, wherein the void ratio $e(r,t)$ is approximated by a sum of N shape functions $\phi_k(r)$ weighted by N nodal values $e_k(t)$:

$$\tilde{e}(r,t) = \sum_{k=1}^{N} e_k(t)\, f_k(r) \quad \text{on } 0 \le r \le R(t), \text{ for } t>0, \tag{4.7}$$

where $\tilde{e}(r,t)$ denotes a finite dimensional approximation of $e(r,t)$.

The expansion (4.7) of the void ratio is introduced in (4.1), which reads now

$$\frac{C}{r}\frac{\partial}{\partial r}\left[r \exp(G\tilde{e})\frac{d f_k}{dr}\right] e_k \approx \frac{1}{1+\tilde{e}}\frac{de_k}{dt}\, f_k \quad \text{on } 0 \le r \le R(t),\ t>0, \tag{4.8}$$

where we used the summation convention introduced by Einstein.

We multiply the governing equation (4.8) by each of the shape functions $\phi_i(r)$ and integrate the products over the space domain bounded by $\Omega(t)=[0,R(t)]$:

$$\int_{\Omega(t)} f_i \left[\frac{C}{r}\frac{\partial}{\partial r}\left(r \exp(G\tilde{e})\frac{d f_k}{dr}\right) e_k \right] 2\pi r dr = \int_{\Omega(t)} f_i \left[\frac{1}{1+\tilde{e}}\frac{de_k}{dt}\, f_k \right] 2\pi r dr\,. \tag{4.9}$$

where $0 \le r \le R(t),\ t>0$,
the integrals are set equal for $1 \le i \le N$.

By integration by parts of the left hand side,

$$\left[\int_{\Omega(t)} f_i \frac{1}{1+\tilde{e}}\, f_k r dr \right] \dot{e}_k + \left[\int_{\Omega(t)} C r \exp(G\tilde{e})\frac{d f_i}{dr}\frac{d f_k}{dr}\, dr \right] e_k = \left[C\, f_i r \exp(G\tilde{e})\frac{d f_k}{dr} e_k \right]_{r=0}^{r=R(t)} \tag{4.10}$$

where the dot symbol denotes the derivative with respect to time,
$0 \le r \le R(t),\ t>0$,
$1 \le i \le N$.

The result of the above (4.10) "weak form" of equation (4.1) is a coupled system of non-linear, first-order ordinary differential equations in time, which can be written in the following compact matrix form:

$$\underline{\underline{M}}(t)\dot{\underline{e}}(t)+\underline{\underline{K}}(t)\underline{e}(t)=\underline{F}(t) \tag{4.11}$$

where
$$\begin{cases} M_{ik}(\underline{e})=\int\limits_{\Omega(t)} f_i \dfrac{1}{1+\tilde{e}} f_k r dr \\ K_{ik}(\underline{e})=\int\limits_{\Omega(t)} Cr\exp(G\tilde{e})\dfrac{d f_i}{dr}\dfrac{d f_k}{dr} dr \ . \\ F_i(\underline{e})=\left[C f_i r\exp(G\tilde{e})\dfrac{d f_k}{dr} e_k \right]_{r=0}^{r=R(t)} \end{cases} \tag{4.12}$$

$\underline{e}(t)$ is the nodal value vector composed of the nodal values $e_k(t)$ $(1\le k\le N)$ of the finite-element approximation of the void ratio,
$0\le r\le R(t)$, $t>0$,
$1\le i,k\le N$.

We determine the motion of the moving boundary by

$$\dot{R} = C\exp(G\tilde{e})\frac{d f_k}{dr}\bigg|_{r=R(t)} e_k \quad \text{for } t>0. \tag{4.13}$$

Equations (4.11) and (4.13) are the set of first-order differential equations that we have to solve.

The internal node motion remains to be defined. We use the following simple law of motion for a node m:

$$r_m(t) = c_m R(t) \text{ for } t>0, \tag{4.14}$$

where c_m are constants, $1\le m\le N$.

Although a wide variety of shape functions could be used, the regularity requirements implied by the Galerkin formulation are that they be at least C^0. We will use linear ones, as represented in Figure **4.1** :

$$f_k(r)=\begin{cases} \dfrac{r-r_{k-1}}{r_k-r_{k-1}} & r\in[r_{k-1};r_k] \\ \dfrac{r_{k+1}-r}{r_{k+1}-r_k} & \textit{for} \quad r\in[r_k;r_{k+1}]. \\ 0 & \textit{otherwise} \end{cases} \tag{4.15}$$

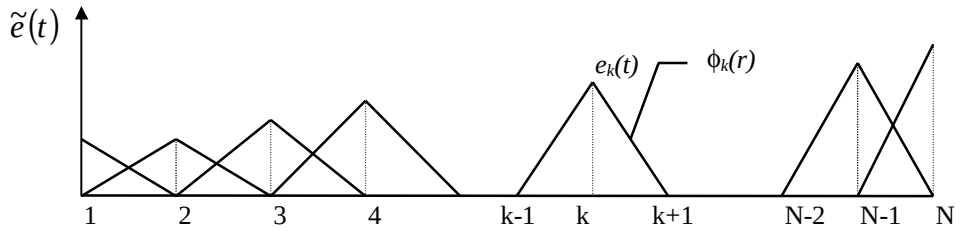

Figure 4.1 Spatial discretization and finite-element approximation of the void ratio.

With these shape functions, the terms of the matrices M_{ik} and K_{ik} in (4.11) are different from 0 only for $k=i$-1, $k=i$ and $k=i$+1. Concerning the right-hand side F_i, they are different from zero only for the extreme term $i=N$. The system of equations (4.11) becomes tridiagonal:

$$\begin{bmatrix} M_{11} & M_{12} & 0 & 0 & 0 \\ M_{21} & M_{22} & M_{23} & 0 & 0 \\ 0 & M_{32} & M_{33} & M_{34} & 0 \\ 0 & 0 & \cdots & \cdots & \cdots \\ 0 & 0 & 0 & M_{NN-1} & M_{NN} \end{bmatrix} \begin{bmatrix} \dot{e}_1 \\ \dot{e}_2 \\ \dot{e}_3 \\ \cdots \\ \dot{e}_N \end{bmatrix} + \begin{bmatrix} K_{11} & K_{12} & 0 & 0 & 0 \\ K_{21} & K_{22} & K_{23} & 0 & 0 \\ 0 & K_{32} & K_{33} & K_{34} & 0 \\ 0 & 0 & \cdots & \cdots & \cdots \\ 0 & 0 & 0 & K_{NN-1} & K_{NN} \end{bmatrix} \begin{bmatrix} e_1 \\ e_2 \\ e_3 \\ \cdots \\ e_N \end{bmatrix} = \begin{bmatrix} 0 \\ 0 \\ 0 \\ \cdots \\ F_N \end{bmatrix} \tag{4.16}$$

and the equation for the motion of the boundary condition (4.13) reads :

$$\dot{R} = C \exp\left(Ge_N\right)\left[\left.\frac{df_{N-1}}{dr}\right|_{r=R(t)} e_{N-1} + \left.\frac{df_N}{dr}\right|_{r=R(t)} e_N\right] \text{ for } t>0. \tag{4.17}$$

4.3 TIME INTEGRATION SCHEME

We solve (4.11) and (4.13) in a decoupled fashion. According to the structure of the matrix M in (4.11), an explicit method could be used to solve the system of equations (4.11). However, we will consider here implicit methods because of their greater stability, which can be used to advantage when an explicit method would impose unrealistically small time steps, a disadvantage that could seriously hinder the deployment of graded meshes since time steps are functions of the smallest mesh size. Unfortunately, this greater stability exacts a significant computational price, since the solution of the system of equations must be obtained once per time step.

The integration scheme developed here is based on two second-order-accurate integration techniques proposed by Gresho *et al.* [1], the explicit Adams-Bashforth formula and the implicit trapezoid rule. By combination of these two common techniques, a stable scheme is obtained in which the temporal accuracy is controlled by automatic time step modification based on a good estimate of the local single step time truncation error. This automatic time step modification provides a cost-effective algorithm in the sense that

the time step is increased whenever possible and decreased only when necessary. The non-linear systems obtained are solved using a Newton-Raphson method, which requires the construction of a linear system. This unsymmetrical linear system is solved via Gaussian elimination.

The overall time integration scheme can be described as follows. From the knowledge of the moving boundary position and the void ratio at time t_n, we predict the moving boundary position and the void ratio at time t_{n+1}. We then solve (4.11) in the predicted domain and finally, we correct the moving boundary position by solving (4.13). More precisely, let $\underline{e}^n$ and R^n be the nodal vector of the void ratio and position of the moving boundary at the time t_n:

$$\underline{e}^n = \underline{e}(t_n) \tag{4.18}$$

$$R^n = R(t_n) \tag{4.19}$$

We obtain the corresponding vector and position at time $t_{n+1}=t_n+\Delta t_n$ after completion of the following steps:

4.3.1 Predictor step

We predict $\underline{e}_{pred}$ and R_{pred} at the time t_{n+1} by means of the variable step, second-order Adams-Bashforth formula:

$$\underline{e}_{pred}^{n+1} = \underline{e}^n + \frac{\Delta t_n}{2}\left[\left(2+\frac{\Delta t_n}{\Delta t_{n-1}}\right)\dot{\underline{e}}^n - \frac{\Delta t_n}{\Delta t_{n-1}}\dot{\underline{e}}^{n-1}\right], \tag{4.20}$$

$$R_{pred}^{n+1} = R^n + \frac{\Delta t_n}{2}\left[\left(2+\frac{\Delta t_n}{\Delta t_{n-1}}\right)\dot{R}^n - \frac{\Delta t_n}{\Delta t_{n-1}}\dot{R}^{n-1}\right]. \tag{4.21}$$

where the time derivatives $\dot{\underline{e}}^n$, $\dot{\underline{e}}^{n-1}$, $\dot{R}^n$ and $\dot{R}^{n-1}$ are known from the previous time steps,
$\Delta t_n=t_{n+1}-t_n$.

This predictor step performs two important functions: it provides a very good predictor for the Trapezoid rule, which contributes substantially to the success of the Newton-Raphson method, and it permits control of the local error. This relatively cheap predictor is thus quite cost-effective.

4.3.2 Relocation of the internal nodes

Relocation of the internal nodes by means of the predicted tip position (4.21) and the law of motion (4.14).

4.3.3 Corrector step

Computation of $\underline{e}^{n+1}$ on the predicted finite-element grid by means of the completely stable implicit Trapezoid rule (Crank-Nicholson). Applied to $\dot{y} = f$, it gives

$$y^{n+1} = y^n + \frac{\Delta t_n}{2}\left(f_n + f_{n+1}\right). \tag{4.22}$$

In order to apply the implicit trapezoidal rule to discretize (4.11) in time, we have to assume that $\underline{\underline{M}}$ is invertible at all times t>0, (4.11) can then be rewritten as

$$\dot{\underline{e}} = \underline{\underline{M}}^{-1}\left(\underline{F} - \underline{\underline{K}}\,\underline{e}\right) \tag{4.23}$$

and the numerical scheme (4.22) reads then

$$\underline{e}^{n+1} = \underline{e}^n + \frac{\Delta t_n}{2}\left(\dot{\underline{e}}^n + \underline{\underline{M}}\left(\underline{e}^{n+1}\right)^{-1}\underline{F}\left(\underline{e}^{n+1}\right) - \underline{\underline{M}}\left(\underline{e}^{n+1}\right)^{-1}\underline{\underline{K}}\left(\underline{e}^{n+1}\right)\underline{e}^{n+1}\right). \tag{4.24}$$

Multiplying by $2/\Delta t_n \underline{\underline{M}}(e^{n+1})$, this equation can be rewritten as a set of algebraic equations in terms of the unknown nodal value vector $\underline{e}^{n+1}$:

$$\left[\frac{2}{\Delta t_n}\underline{\underline{M}}\left(\underline{e}^{n+1}\right) + \underline{\underline{K}}\left(\underline{e}^{n+1}\right)\right]\underline{e}^{n+1} = \left[\underline{\underline{M}}\left(\underline{e}^{n+1}\right)\left(\frac{2}{\Delta t_n}\underline{e}^n + \dot{\underline{e}}^n\right) + \underline{F}\left(\underline{e}^{n+1}\right)\right] \tag{4.25}$$

where the time derivative $\dot{\underline{e}}^n$ of the nodal value vector and the nodal value vector at the previous time step is used,
the integrals in the matrices $\underline{\underline{M}}$, $\underline{\underline{K}}$ and vector $\underline{F}$ are evaluated on the predicted domain $0 \le r \le R_{pred}^{\,n+1}$.

We recognize equation (4.25) as a nonlinear algebraic system $\underline{\underline{A}}(\underline{x})\underline{x} = \underline{b}(\underline{x})$. Calculation of the void ratio field based on this system of equations is the most costly operation in terms of computer time for it involves the solution of a large nonlinear system. We solve it by the Newton-Raphson iterative technique with predicted values of *e* and *R* as first estimates. This method is quite powerful in time-dependent problems because good first guesses are always available, especially when it is coupled with a predictor equation. The use of predicted values as first estimates in the iterative process is so efficient that a single iteration of Newton's method is usually sufficient for achieving full convergence. Newton-Raphson requires the construction of a linear system. In the case of $A_{ij}\left(\underline{x}\right)x_j - b_i\left(\underline{x}\right) = 0$, where a predictor $\underline{x}_{pred}$ is available for the vector $\underline{x}$, the linear system of equations reads:

$$A_{ij}\left(\underline{x}_{pred}\right)x_{j,pred} - b_i\left(\underline{x}_{pred}\right) + \frac{d}{dx_j}\left[A_{ik}\left(\underline{x}\right)x_{k,pred} - b_i\left(\underline{x}\right)\right]\Big|_{\underline{x}=\underline{x}_{pred}}\left(x_j - x_{j,pred}\right) = 0 \tag{4.26}$$

or

$$J_{ij}\left(\underline{x}_{pred}\right)\left(x_j - x_{j,pred}\right) = b_i\left(\underline{x}_{pred}\right) - A_{ij}\left(\underline{x}_{pred}\right)x_{j,pred} \tag{4.27}$$

where x_j are the unknowns, $1 \le j \le N$,
$J_{ij}(\underline{x})$ is the Jacobian matrix of $A_{ik}(\underline{x})x_k - b_i(\underline{x})$, (4.28)
$1 \le i \le N$.

The system of equations (4.27) is commonly solved for $\Delta x_j = x_j - x_{j,pred}$, $1 \le j \le N$. The values x_j are then computed as $x_j = x_{j,pred} + \Delta x_j$. The Jacobian matrix (4.28) has to be evaluated for $\underline{x} = \underline{x}_{pred}$. We thus have

$$J_{ij}\left(\underline{x}_{pred}\right) = A_{ij}\left(\underline{x}_{pred}\right) + \frac{dA_{ik}(\underline{x})}{dx_j} x_{k,pred}\bigg|_{\underline{x}=\underline{x}_{pred}} - \frac{db_i(\underline{x})}{dx_j}\bigg|_{\underline{x}=\underline{x}_{pred}}, \qquad (4.29)$$

where $1 \le i, j \le N$

In the case of the system of equations (4.25), we have to determine the unknown vector $\underline{e}^{n+1}$. The matrix $\underline{\underline{A}}$ and vector $\underline{b}$ read respectively

$$A_{ij} = \frac{2}{\Delta t_n} M_{ij}\left(\underline{e}^{n+1}\right) + K_{ij}\left(\underline{e}^{n+1}\right) \qquad (4.30)$$

and

$$b_i = M_{ij}\left(\underline{e}^{n+1}\right)\left(\frac{2}{\Delta t_n} e_j^n + \dot{e}_j^n\right) + F_i\left(\underline{e}^{n+1}\right). \qquad (4.31)$$

The Jacobian $\underline{J}$ of (4.28) reads thus in our case

$$J_{ij}\left(\underline{e}_{pred}^{n+1}\right) = \begin{cases} \dfrac{2}{\Delta t_n} M_{ij}\left(\underline{e}_{pred}^{n+1}\right) + K_{ij}\left(\underline{e}_{pred}^{n+1}\right) + \dfrac{2}{\Delta t_n}\dfrac{d}{de_j^{n+1}} M_{ik}\left(\underline{e}^{n+1}\right)\Big|_{\underline{e}^{n+1}=\underline{e}_{pred}^{n+1}} e_{k,pred}^{n+1} + \\ \dfrac{d}{de_j^{n+1}} K_{ij}\left(\underline{e}^{n+1}\right)\Big|_{\underline{e}^{n+1}=\underline{e}_{pred}^{n+1}} e_{k,pred}^{n+1} - \dfrac{d}{de_j^{n+1}} M_{ik}\left(\underline{e}^{n+1}\right)\Big|_{\underline{e}^{n+1}=\underline{e}_{pred}^{n+1}} \\ \left(\dfrac{2}{\Delta t_n} e_k^n + \dot{e}_k^n\right) - \dfrac{d}{de_j} F_i\left(\underline{e}^{n+1}\right)\Big|_{\underline{e}^{n+1}=\underline{e}_{pred}^{n+1}} \end{cases} \qquad (4.32)$$

or, by grouping terms,

$$J_{ij}\left(\underline{e}_{pred}^{n+1}\right)=\begin{cases}\dfrac{2}{\Delta t_n}M_{ij}\left(\underline{e}_{pred}^{n+1}\right)+K_{ij}\left(\underline{e}_{pred}^{n+1}\right)+\\ \dfrac{2}{\Delta t_n}\dfrac{d}{de_j^{n+1}}M_{ik}\left(\underline{e}^{n+1}\right)\Big|_{\underline{e}^{n+1}=\underline{e}_{pred}^{n+1}}\left(e_{k,pred}^{n+1}-e_k^n-\dfrac{\Delta t_n}{2}\dot{e}_k^n\right)+\\ \dfrac{d}{de_j^{n+1}}K_{ij}\left(\underline{e}^{n+1}\right)\Big|_{\underline{e}^{n+1}=\underline{e}_{pred}^{n+1}}e_{k,pred}^{n+1}-\dfrac{d}{de_j^{n+1}}F_i\left(\underline{e}^{n+1}\right)\Big|_{\underline{e}^{n+1}=\underline{e}_{pred}^{n+1}}\end{cases} \qquad (4.33)$$

The system of equations (4.27) can thus be written as

$$\left[\frac{2}{\Delta t_n}M_{ij}\left(\underline{e}_{pred}^{n+1}\right)+K_{ij}\left(\underline{e}_{pred}^{n+1}\right)-\frac{2}{\Delta t_n}L_{ij}\left(\underline{e}_{pred}^{n+1}\right)+N_{ij}\left(\underline{e}_{pred}^{n+1}\right)-\frac{\partial F_i\left(\underline{e}^{n+1}\right)}{\partial e_j^{n+1}}\Big|_{\underline{e}=\underline{e}_{pred}^{n+1}}\right]\left[e_j^{n+1}-e_{j,pred}^{n+1}\right]=$$
$$\left[M_{ij}\left(\underline{e}_{pred}^{n+1}\right)\left(\frac{2}{\Delta t_n}e_j^n+\dot{e}_j^n\right)+F_i\left(\underline{e}_{pred}^{n+1}\right)\right]-\left[\frac{2}{\Delta t_n}M_{ij}\left(\underline{e}_{pred}^{n+1}\right)+K_{ij}\left(\underline{e}_{pred}^{n+1}\right)\right]e_{j,pred}^{n+1} \qquad (4.34)$$

where $1\le i\le N$,

$$\begin{cases}L_{ij}\left(\underline{e}_{pred}^{n+1}\right)=\int\limits_{\Omega(t_{n+1})}f_i\dfrac{r}{\left(1+\tilde{e}_{pred}^{n+1}\right)^2}f_j f_k dr\left(e_{k,pred}^{n+1}-e_k^n-\dfrac{\Delta t_n}{2}\dot{e}_k^n\right)\\ N_{ij}\left(\underline{e}_{pred}^{n+1}\right)=\int\limits_{\Omega(t_{n+1})}\dfrac{df_i}{dr}CrG\,f_j\exp\left(G\tilde{e}_{pred}^{n+1}\right)\dfrac{df_k}{dr}dre_{k,pred}^{n+1}\\ F_i\left(\underline{e}_{pred}^{n+1}\right)=\left[C\,f_i r\exp\left(G\tilde{e}_{pred}^{n+1}\right)\dfrac{df_k}{dr}e_{k,pred}^{n+1}\right]_{r=0}^{r=R(t_{n+1})}\end{cases}. \qquad (4.35)$$

The elements of the matrices $\underline{K}$, $\underline{L}$, $\underline{M}$, $\underline{N}$ are different from zero only for $j=i$-1, $j=i$ *and* $j=i$+1. Concerning the derivatives of $\underline{F}$ with respect to e_j^{n+1}, two elements only are different from zero: $i=N$, $j=N$-1 and $i=N$, $j=N$. Concerning the vector $\underline{F}$ itself, its elements are different f3rom zero only for $i=N$.

Since the boundary condition (4.6) imposes the value of the last nodal value e_N, the predictor $e_{N,pred}^{n+1}$ is set equal to e_{limit} and $e_N^{n+1}-e_{N,pred}^{n+1}$ is set equal to zero for the solution of the system of N equations and N unknowns (4.34). Using this last equality, this system can be reduced to a system of N-1 equations and N-1 unknowns by removing the last line *(i=N)* and last column *(j=N)* of the Jacobian $\underline{J}$ and the last element *(i=N)* of the

right-hand side of (4.34). Thus, neither $\underline{F}$ nor its derivatives with respect to e_j^{n+1} have to be computed.

The solution of the reduced system usually does not require more than one iteration. However, if the user-specified convergence criterion on the nodal values of the void ratio is not reached after one iteration, we proceed to subsequent iterations. In this case, the matrices $\underline{\underline{K}}$, $\underline{\underline{L}}$, $\underline{\underline{M}}$, $\underline{\underline{N}}$ in (4.34) are recalculated on the same spatial domain but with the most recent $\underline{e}^{n+1}$ instead of $\underline{e}_{pred}^{n+1}$.

4.3.4 Correction of the moving boundary position

We correct the moving boundary position R with the void ratio nodal vector $\underline{e}^{n+1}$ found in step (c). Applying the Trapezoid rule, the time discretization of (4.13) leads to

$$R^{n+1} = R^n + \frac{\Delta t_n}{2}\left[C \exp\left(G\tilde{e}^{\,n}\right)\frac{d f_k}{dr}\bigg|_{r=R(t_n)} e_k^n + C \exp\left(G\tilde{e}^{\,n+1}\right)\frac{d f_k}{dr}\bigg|_{r=R(t_{n+1})} e_k^{n+1}\right] \tag{4.36}$$

The relative difference between the previous and new tip positions R^n and R^{n+1} respectively may be larger than the user-specified convergence criterion. In this case, subsequent iterations through (b), (c) and (d) are necessary. For step (b), the most recent tip position R^{n+1} is used to relocate the internal nodes. Then, the matrices $\underline{\underline{K}}$, $\underline{\underline{L}}$, $\underline{\underline{M}}$, $\underline{\underline{N}}$ in (4.34) are recalculated on the new spatial domain $[0,R^{n+1}]$ instead of $[0,R_{pred}^{n+1}]$ with the second most recent $\underline{e}^{n+1}$ instead of $\underline{e}_{pred}^{n+1}$. Afterwards, "inner"-iterations are performed on (4.34) to solve for $\underline{e}^{n+1}$ step (c) and the tip position is corrected in step (d). These "outer"-iterations are performed until the user-specified convergence criterion on the tip position is fulfilled.

4.3.5 Evaluation of the time derivatives

The time derivatives to be used in step (a) at the next time step have to be evaluated. This is conveniently done by inversion of the Trapezoid rule:

$$\dot{\underline{e}}^{n+1} = \frac{2}{\Delta t_n}\left(\underline{e}^{n+1} - \underline{e}^{n}\right) - \dot{\underline{e}}^{n}, \tag{4.37}$$

$$\dot{R}^{n+1} = \frac{2}{\Delta t_n}\left(R^{n+1} - R^{n}\right) - \dot{R}^{n}. \tag{4.38}$$

where $\dot{\underline{e}}^{n}$ is available from the previous application of the same equation.

4.3.6 Computation of the next time step

An automatic selection of the time increment is made during the simulation, on the basis of the difference between the predicted and corrected values and user-specified level of local time truncation error. The estimation of the local time truncation error begins

with a Taylor series analysis of both predictor and corrector schemes. Denoting $y(t_n)$ the exact solution at time t_n and assuming that the exact solution is known at the beginning of the time step, i.e. $y^n=y(t_n)$, we have the following error estimate for the predictor :

$$y_{pred}^{n+1} - y(t_{n+1}) =$$
$$y^n + \frac{\Delta t_n}{2}\left[\left(2+\frac{\Delta t_n}{\Delta t_{n-1}}\right)\dot{y}^n - \frac{\Delta t_n}{\Delta t_{n-1}}\dot{y}^{n-1}\right] - \left(y^n + \Delta t_n \dot{y}^n + \frac{\Delta {t_n}^2}{2}\ddot{y}^n + \frac{\Delta {t_n}^3}{6}\dddot{y}^n + O\left(\Delta {t_n}^4\right)\right) =$$
$$-\frac{\Delta {t_n}^3}{6}\dddot{y}^n + \frac{\Delta {t_n}^2}{2}\left(\dot{y}^n - \dot{y}^{n-1}\right)\frac{1}{\Delta t_{n-1}} - \frac{\Delta {t_n}^2}{2}\ddot{y}^n + O\left(\Delta {t_n}^4\right) \tag{4.39}$$

Introducing the following Taylor series

$$\dot{y}^n = \dot{y}^{n-1} + \Delta t_{n-1}\ddot{y}^{n-1} + \frac{\Delta {t}^2_{n-1}}{2}\dddot{y}^{n-1} + O\left(\Delta t_{n-1}^3\right), \tag{4.40}$$

the second term of the right-hand side of (4.39) can be modified using

$$\left(\dot{y}^n - \dot{y}^{n-1}\right)\frac{1}{\Delta t_{n-1}} = \ddot{y}^{n-1} + \frac{\Delta t_{n-1}}{2}\dddot{y}^{n-1} + O\left(\Delta t_{n-1}^2\right). \tag{4.41}$$

Replacing the second and third derivatives of y with respect to time in (4.41) by their Taylor series, equation (4.41) reads now

$$\frac{\dot{y}^n - \dot{y}^{n-1}}{\Delta t_{n-1}} =$$
$$\left(\ddot{y}^n - \Delta t_{n-1}\dddot{y}^n + O\left(\Delta t_{n-1}^2\right)\right) + \frac{\Delta t_{n-1}}{2}\left(\dddot{y}^n + O\left(\Delta t_{n-1}\right)\right) + O\left(\Delta t_{n-1}^2\right) = \tag{4.42}$$
$$\ddot{y}^n - \frac{\Delta t_{n-1}}{2}\dddot{y}^n + O\left(\Delta t_{n-1}^2\right)$$

The truncation error (4.39) for the predictor becomes then

$$y_{pred}^{n+1} - y(t_{n+1}) = -\frac{1}{12}\left(2+3\frac{\Delta t_{n-1}}{\Delta t_n}\right)\Delta {t_n}^3\dddot{y}^n + O\left(\Delta {t_n}^4\right) \tag{4.43}$$

Concerning the corrector step, we have

$$y_{n+1} - y(t_{n+1}) =$$
$$y^n + \frac{\Delta t_n}{2}\left(\dot{y}^n + \dot{y}^{n+1}\right) - \left(y^n + \Delta t_n \dot{y}^n + \frac{\Delta {t_n}^2}{2}\ddot{y}^n + \frac{\Delta {t_n}^3}{6}\dddot{y}^n + O\left(\Delta {t_n}^4\right)\right) = \tag{4.44}$$
$$\frac{\Delta t_n}{2}\left(\dot{y}^{n+1} - \dot{y}^n\right) - \frac{\Delta {t_n}^2}{2}\ddot{y}^n - \frac{\Delta {t_n}^3}{6}\dddot{y}^n + O\left(\Delta {t_n}^4\right)$$

Expanding $\dot{y}^{n+1}$ in a Taylor series, the truncation error on the corrector becomes

$$d\left(y^{n+1}\right)= y^{n+1} - y\left(t_{n+1}\right)= \frac{\Delta t_n{}^3}{12}\,\dddot{y}^n + O\left(\Delta t_n{}^4\right) \tag{4.45}$$

where $d\left(y^{n+1}\right)= y^{n+1} - y\left(t_{n+1}\right)$ is the estimate of the local time truncation error of the actual solution. This expression contains the unknowns $y\left(t_{n+1}\right)$ and $\dddot{y}^n$. However, we can express (4.45) in terms of the known variables y_{pred}^{n+1} and y^{n+1} by substituting $\dddot{y}^n$ from (4.45) into (4.43):

$$d\left(y^{n+1}\right)= \frac{y^{n+1} - y_{pred}^{n+1}}{3\left(1+\dfrac{\Delta t_{n-1}}{\Delta t_n}\right)} + O\left(\Delta t_n^4\right). \tag{4.46}$$

This result can be used to estimate the next time step Δt_{n+1} based on the requirement that a relative norm of the error for the next time step should equal a pre-set input value ε. From equation (4.45), we have

$$\frac{\left|d\left(y^{n+2}\right)\right|}{\left|d\left(y^{n+1}\right)\right|} = \left(\frac{\Delta t_{n+1}}{\Delta t_n}\right)^3 \frac{\left|\dddot{y}^{n+1}\right|}{\left|\dddot{y}^n\right|} \tag{4.47}$$

Since $\dddot{y}^{n+1} = \dddot{y}^n + O\left(\Delta t_n\right)$, equation (4.47) permits the solution for Δt_{n+1}, after setting $\left|d\left(y^{n+2}\right)\right| = e$ and neglecting higher-order terms:

$$\Delta t_{n+1} = \Delta t_n \left(\frac{e}{\left|d\left(y^{n+1}\right)\right|}\right)^{1/3} \tag{4.48}$$

is used to compute the next time step.

In our work, we have been using the following norm proposed by Gresho *et al.*[1] for the error estimates:

$$\left|d\left(y^{n+1}\right)\right|^2 = \frac{1}{N+1}\frac{1}{\left[3\left(1+\dfrac{\Delta t_{n-1}}{\Delta t_n}\right)\right]^2}\left[\frac{1}{\left(e_{\max}^{n+1}\right)^2}\sum_{i=1}^{N}\left(e_i^{n+1} - e_{i,\,pred}^{n+1}\right)^2 + \frac{1}{\left(R^{n+1}\right)^2}\left(R^{n+1} - R_{pred}^{n+1}\right)^2\right] \tag{4.49}$$

The entire algorithm for advancing the solution by one time step can be summarized as follows:

1. the predictors for the nodal vector of the void ratio and the moving boundary position are computed,

2. the internal nodes are relocated,

3. the Jacobian matrix and the right-hand side of (4.27) are assembled by looping through the elements,

4. the nodal vector of the void ratio is computed by solving the linear system,

5. the position of the moving boundary is corrected,

6. the nodal vector of the void ratio change rate and the change rate of the moving boundary position is computed for the next time step,

7. the next time step is computed.

The only user-specified parameter is ε in (4.48). It has been chosen equal to *0.001* in this work.

The convergence criterion on the Newton- Raphson iterative scheme for the void ratio is based on the norm of the vector of the relative error between two successive iterations and has to be less than $0.1 \cdot \varepsilon$. The same convergence criterion is imposed on the moving boundary position.

Concerning the time step modification, we always accept the increase if $\Delta t_{n+1} \geq 0.8 \cdot \Delta t_n$ but repeat the time step with $\Delta t_n = \Delta t_{n+1}$ otherwise.

4.4 INITIALIZATION

Since $\underline{\dot{e}}^{n-1}$ and $\dot{R}^{n-1}$ are required in the equations (4.20) and (4.21), the method above can not be applied until the third time step. The two first time steps require a special treatment.

4.4.1 Computation of the first time step

For the first time step n=0, we do not use a predictor-corrector method with automatic time-step modification. The nodal values of the void ratio and the tip position are evaluated at the time t_1 with the first-order Euler Backward scheme. Applied to $\dot{y} = f$, the scheme reads

$$y^1 = y^0 + \Delta t_0 f^1 . \tag{4.50}$$

Applied to our problem, we have the following non-linear algebraic system of equations

$$\left[\frac{1}{\Delta t_0} \underline{\underline{M}}\left(\underline{e}^1\right) + \underline{\underline{K}}\left(\underline{e}^1\right) \right] \underline{e}^1 = \left[\frac{1}{\Delta t_0} \underline{\underline{M}}\left(\underline{e}^1\right) \underline{e}^0 + \underline{F}\left(\underline{e}^1\right) \right], \tag{4.51}$$

where the integrals in $\underline{\underline{M}}$, $\underline{\underline{K}}$ and $\underline{F}$ - see equation (4.12) - are evaluated on the initial domain $[0;R_0]$.

Newton-Raphson iterative technique is used to solve this set of equations. The algebraic system of linear equations reads

$$\left[\frac{1}{\Delta t_0} M_{ij}\left(\underline{e}^1_{pred}\right) + K_{ij}\left(\underline{e}^1_{pred}\right) - \frac{1}{\Delta t_0} L_{ij}\left(\underline{e}^1_{pred}\right) + N_{ij}\left(\underline{e}^1_{pred}\right) - \left.\frac{\partial F_i\left(\underline{e}^1\right)_i}{\partial e^1_j}\right|_{\underline{e}^1=\underline{e}^1_{pred}}\right]\left[e^1_j - e^1_{j,pred}\right] =$$

$$\left[M_{ij}\left(\underline{e}^1_{pred}\right)\frac{1}{\Delta t_0} e^0_j + F_i\left(\underline{e}^1_{pred}\right)\right] - \left[\frac{1}{\Delta t_0} M_{ij}\left(\underline{e}^1_{pred}\right) + K_{ij}\left(\underline{e}^1_{pred}\right)\right] e^1_{j,pred} \tag{4.52}$$

where $1 \le i \le N$,

the first guess for the nodal values $e^1_{j,\,pred}$ will be the initial conditions except for $e^1_{N,\,pred}$, which is given by the boundary condition e_{limit}.

The position of the moving boundary is given by the same numerical scheme (4.50):

$$R^1 = R^0 + \Delta t_0 C \exp\left(G\tilde{e}^1\right)\left.\frac{d f_k}{dr}\right|_{r=R(t_1)} e^1_k \,. \tag{4.53}$$

Concerning the convergence on the void ratio and on the tip position, the same remarks as in the general case for $n>1$ apply. The time derivatives to be used in the next time step have to be evaluated. This is conveniently done by inversion of the Euler Backward scheme:

$$\dot{\underline{e}}^1 = \frac{1}{\Delta t_0}\left(\underline{e}^1 - \underline{e}^0\right), \tag{4.54}$$

$$\dot{R}^1 = \frac{1}{\Delta t_0}\left(R^1 - R^0\right). \tag{4.55}$$

As no automatic modification of the next time step is available for this scheme, the next time step will be given by

$$\Delta t_1 = \Delta t_0 \,. \tag{4.56}$$

4.4.2 Computation of the second time step

For the second time step $n=1$, the predictor (4.20) is not applicable because it requires two history vectors of acceleration. A predictor-corrector of lower order than the Adams-Bashforth/Trapezoid rule scheme is used to modify automatically the time step. The steps (a) through (e) are essentially similar to those of the general case, except that

the Adams-Bashforth rule is replaced by the Euler Forward rule for the predictor, the Trapezoid rule by the Euler Backward rule for the corrector and the inverted Trapezoid rule by the inverted Euler Backward rule for the evaluation of the time derivatives. Applied to $\dot{y} = f$, the new rules read respectively

$$y^2_{pred} = y^1 + \Delta t_1 \dot{y}^1, \tag{4.57}$$

$$y^2 = y^1 + \Delta t_1 f^2 \text{ and} \tag{4.58}$$

$$\dot{y}^2 = \frac{1}{\Delta t_1}\left(y^2 - y^1\right). \tag{4.59}$$

Based on the same requirements as before, the third time step Δt_2 can be estimated using the following equation

$$\Delta t_2 = \Delta t_1 \left(\frac{e}{\left| d\left(y^2\right) \right|} \right)^{1/2} \tag{4.60}$$

where $\left| d\left(y^2\right) \right|^2 = \frac{1}{N+1}\frac{1}{4}\left[\frac{1}{\left(e^2_{\max}\right)^2} \sum_{i=1}^{N} \left(e_i^2 - e_{i,pred}^2\right)^2 + \frac{1}{\left(R^2\right)^2}\left(R^2 - R^2_{pred}\right)^2 \right]$ (4.61)

4.5 REFERENCES FOR CHAPTER 4

[1] P.M. Gresho, R.L. Lee, R.L. Sani, *Recent Advances in Numerical Methods in Fluids*, Pineridge Press, 1980.

CHAPTER

FIVE

VALIDATION USING TERZAGHI'S ANALYTICAL SOLUTION

In this chapter, we will derive Terzaghi's analytical solution in a cylindrical geometry and compare this solution with the results given by our numerical scheme, using the same material properties.

5.1 TERZAGHI'S CONSOLIDATION THEORY

Terzaghi's consolidation theory [1] is based on equation (2.5), which can be differentiated with respect to the time and written as

$$\frac{\partial p_w}{\partial t} = -\frac{\partial s'}{\partial t}, \tag{5.1}$$

since the total stress is considered equal everywhere. The effective pressure decrease $\frac{\partial s'}{\partial t}$ per unit time causes an increase of the clay thickness Δs. The relationship between Δs and $\Delta s'$ is given by

$$\Delta s = \frac{V_{total} - V_{total}^0}{V_{total}^0} = \frac{V_{void} - V_{void}^0}{V_{void}^0 + V_{solid}^0} = -\frac{a_v}{1+e_0}\left(s' - s_0'\right) \tag{5.2}$$

where $a_v = -\frac{e - e_0}{s' - s_0'}$. (5.3)

The coefficient of swelling a_v gives the void ratio increase due to an effective pressure drop from its initial value s_0' to its equilibrium value s'. As a_v was a function of the void ratio e in the theory developed in the previous chapter, the first version of the consolidation theory considered a constant value for a_v. This restriction on the equation of state for a_v has to be applied in order to obtain analytical solutions to the problem. With the definition of m_v,

$$m_v = \frac{a_v}{1+e_0}, \tag{5.4}$$

equation (5.2) can be rewritten as

$$\Delta s = -m_v \Delta s'. \tag{5.5}$$

Hence, with equation (5.5), (5.1) becomes

$$m_v \frac{\partial p_w}{\partial t} = \frac{\partial s}{\partial t}, \tag{5.6}$$

which represents the volume of water picked up by a unit volume element per unit time. If we take an infinitely small volume element dV of thickness dz at a depth d-z in Figure 2.7,

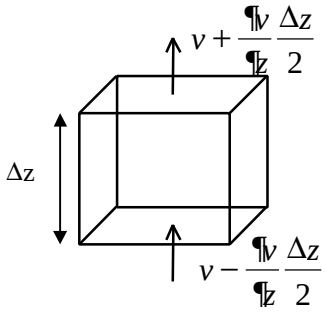

Figure 5.1 Infinitesimally small volume element.

the volume of water taken up per unit time is

$$-\frac{\partial s}{\partial t} dz = -m_v \frac{\partial p_w}{\partial t} dz . \tag{5.7}$$

The water picked up per unit time and area is also equal to the difference between the water volumes flowing out and into dV:

$$\frac{\partial v_z}{\partial z} dz . \tag{5.8}$$

Equating both relations, we get

$$\frac{\partial v_z}{\partial t} = -m_v \frac{\partial p_w}{\partial t} . \tag{5.9}$$

The water flows from the location where the water level in the tubes is high to where it is low. The velocity v_z is given by Darcy's law (3.4):

$$v_z = -\frac{k \rho_w g}{\mu} \frac{\partial h}{\partial z} = -\frac{k}{\mu} \frac{\partial p_w}{\partial z} . \tag{5.10}$$

where we used equation (3.5).

Introducing now the coefficient $c_v = \frac{k}{\rho_w g m_v}$, the continuity relationship (5.9) reads

$$\frac{\partial p_w}{\partial t} = c_v \frac{\partial^2 p_w}{\partial z^2} . \tag{5.11}$$

This equation is of the diffusion-type, for which analytical solutions exist when c_v is constant. Even though the equation (5.11) can not be solved analytically on a time-dependent domain and will thus be solved on the initial domain *[*0; R_0*]* at any time *t*, the volume increase can be computed as a function of time with an expression similar to (5.2) using the infinitesimal thickness increase

$$\Delta s(r,t) = \frac{d\Delta V_{total}(r,t)}{\Delta V_{total}(r,0)} = \frac{e(r,t) - e_0}{1 + e_0} . \tag{5.12}$$

The total volume increase reads now

$$\Delta V_{total}(t) = 2\pi L \int_0^{R_0} \Delta s(r,t) r dr . \tag{5.13}$$

5.2 ANALYTICAL SOLUTION

To be able to compare the results of the numerical simulations with the analytical solution, Terzaghi's problem has to be solved in the same geometry as the one represented in Figure **3.3** Equation (5.11) is rewritten in a cylindrical coordinate system with the same side-conditions as (4.3) to (4.6). The problem is solved in terms of *e* instead of p_w using equation (5.3), in order to relate it more easily to the governing equation (4.1) of our model.

Governing equation:

$$\frac{k}{m a_v} \frac{1}{r} \frac{\partial}{\partial r} \left(r \frac{\partial e}{\partial r} \right) = \frac{1}{1 + e_0} \frac{\partial e}{\partial t} \text{ on } 0 \le r \le R_0. \tag{5.14}$$

Initial conditions:

$$e(r,0) = e_0 \text{ on } 0 \le r \le R_0. \tag{5.15}$$

Boundary conditions:

$$\frac{\partial e}{\partial r} = 0 \text{ for } r=0, \tag{5.16}$$

$$e = e_{\text{limit}} \text{ for } r=R_0. \tag{5.17}$$

The governing equation is solved on the initial domain *[*0 ; R_0*]* at any time. An analytical solution to this problem exists for constant parameters *k*, μ and a_v:

$$e(r,t) = e_0 + (e_{\text{limit}} - e_0)\left[1 - 2\sum_{n=0}^{\infty} \frac{1}{n_n} \frac{J_0\left(n_n \frac{r}{R_0}\right)}{J_1(n_n)} \exp\left[-\left(\frac{n_n}{R_0}\right)^2 \frac{K}{rga_v}(1+e_0)t\right]\right], \quad (5.18)$$

where the ν_n are the zeros of the 0 th order Bessel function of the first kind.

According to equation (5.13) and (3.38), the tip position is

$$R(t) = R_0\sqrt{1 + \frac{e_{\text{limit}} - e_0}{1+e_0}\left[1 - 4\sum_{n=0}^{\infty} \frac{1}{{n_n}^2} \exp\left[-\left(\frac{n_n}{R_0}\right)^2 \frac{K}{rga_v}(1+e_0)t\right]\right]}, \quad (5.19)$$

For t approaching infinity, the infinite summation goes to zero and the tip position $R(t)$ tends to the expression (3.39). The first term in the infinite series tends to dominate as the time increases and will thus dictate the expansion rate of the bentonite. The argument of its exponential has the dimensions of inverse time. The bentonite expansion will thus be characterized by the following characteristic time:

$$t = \left(\frac{R_0}{n_0}\right)^2 \frac{rga_v}{K(1+e_0)} \quad (5.20)$$

which is linearly proportional to the coefficient of compressibility a_v, inversely proportional to the hydraulic conductivity K and $(1+e_0)$ and quadratically proportional to ${R_0}^2$.

5.3 COMPARISON WITH THE NUMERICAL SIMULATIONS

In order to compare the numerical results with the analytical ones, the material properties have to be identical. Since the analytical solution imposes constant material properties, the numerical simulations will be run with constant permeability and constant coefficient of swelling. This can be done by replacing the constants C and G in the governing equations (4.1) and (4.2) by $C = \frac{k_0}{ma_v}$ and $G = 0$. Two major differences remain after imposing constant material properties. The first one is that Terzaghi's governing equation is solved on the initial domain at any time as in our model the domain increases as time goes on. The consequence is that it neglects the bentonite swelling effect on the void ratio gradient at the tip. As the domain swells, the void ratio gradient at the tip will decrease and less water will be absorbed, which will in turn decrease the expansion rate. In that respect, Terzaghi's expansion should be faster than the numerical one. The second difference is that the right-hand sides of the governing equations (4.1) and (5.14) are divided by $1+e(r,t)$ and $1+e_0$ respectively.

However, for e_{limit} approaching e_0, the two differences become negligible. Indeed, the domain size *R(t)* will vary in a very small range, from R_0 to $\lim_{t\to\infty} R(t) = R_0\sqrt{\frac{1+e_{\text{limit}}}{1+e_0}} \approx R_0$ according to (3.39). And on the other hand, *1+e(r,t)* will tend to $1+e_0$ at any time and location. Thus, we should expect the curves to overlap for $e_{limit}=e_0$ and to get closer to each other as e_{limit} approaches e_0.

Figure **5.2**. compares the bentonite expansion obtained by the numerical simulation and Terzaghi's analytical formula (5.19) for the following parameters :

Material properties:

$K = 10^{-13} m/s$ $\qquad$ $a_v = 6.81\cdot 10^{-7}$

Initial and tip void ratios:

$e_0 = 2.0$ $\qquad$ $e_{\text{limit}} = 3.0$

Initial tip position:

$R_0 = 1.0$ m

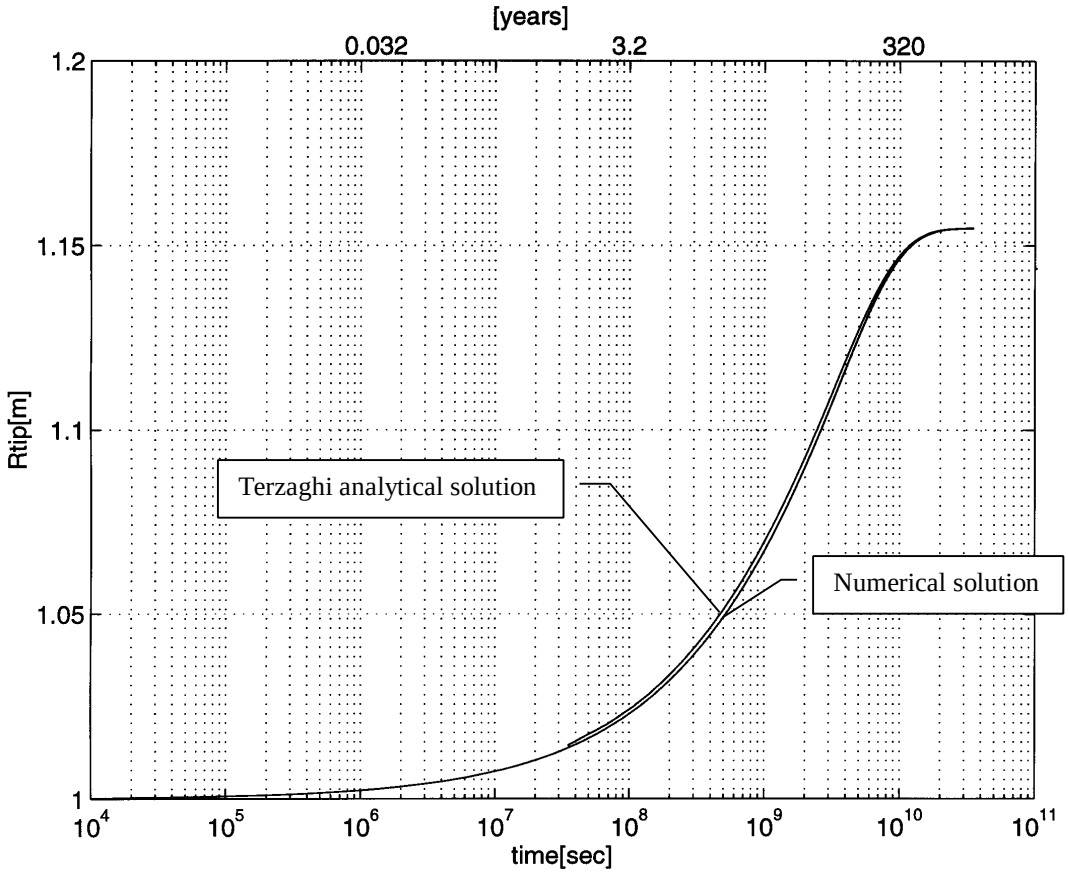

Figure 5.2 Bentonite expansion as a function of time, numerical and analytical results.

The good agreement between the two curves validates in some sort the numerical algorithm used. Solutions have been compared for different values of e_{limit}, the material properties and e_0 being held constant. As e_{limit}, approaches e_0, the curves get closer to each other.

5.4 REFERENCES FOR CHAPTER 5

[1] K. Terzaghi, Erdbaumechanik auf bodenphysikalischer Grundlage, Leipzig und Wien, F. Deuticke, 1925.

CHAPTER
SIX

SENSITIVITY STUDY

In this chapter, we will study the sensitivity of bentonite swelling to hydraulic conductivity, coefficient of swelling, initial void ratio and void ratio at the tip. A survey of the existing literature gave us some values for the hydraulic conductivity and the coefficient of swelling. The results show a rather fast bentonite expansion. An analysis of the differences between the model and the reality is included.

6.1 PARAMETERS LIST FOR THE NUMERICAL SIMULATIONS

A survey of the literature has been done to find typical values for the bentonite hydraulic conductivity and coefficient of swelling. They are summarized in the following tables and depicted in the corresponding graphs. The underlined values correspond to the reference case.

	K_0 [m/s]	C_k [-]
Low hydraulic conductivity	$1.7 \cdot 10^{-14}$	3.125
Average hydraulic conductivity	$\underline{2.3 \cdot 10^{-14}}$	<u>2.26</u>
High hydraulic conductivity	$4.4 \cdot 10^{-14}$	1.40

Table 6.1 K_0 and C_k calculated from R.Pusch [1], p. 104.

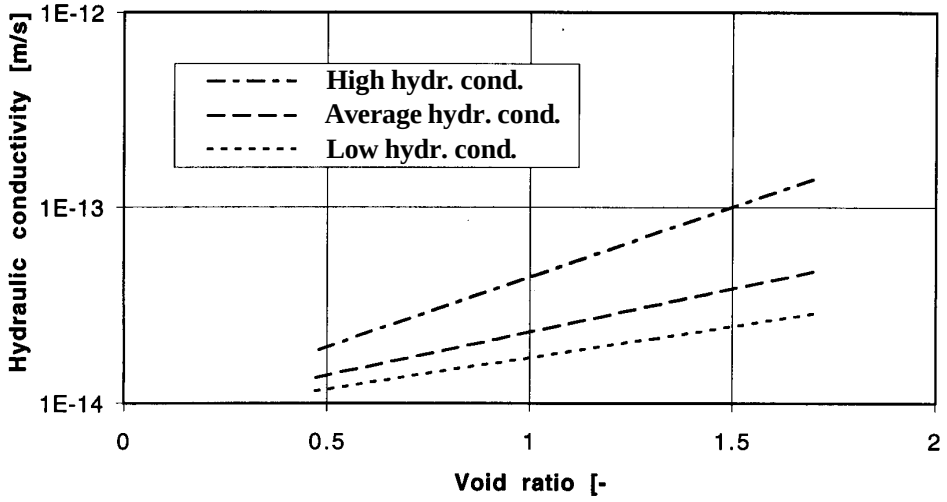

Figure 6.1 Hydraulic conductivity as a function of the void ratio *e*.

	σ'_0 [MPa]	C_s [-]
Swelling case 1	3.16	3.60
Swelling case 2	3.6	1.53

Table 6.2 *s'₀* and C_s calculated from J.K. Mitchell [2], p. 295.

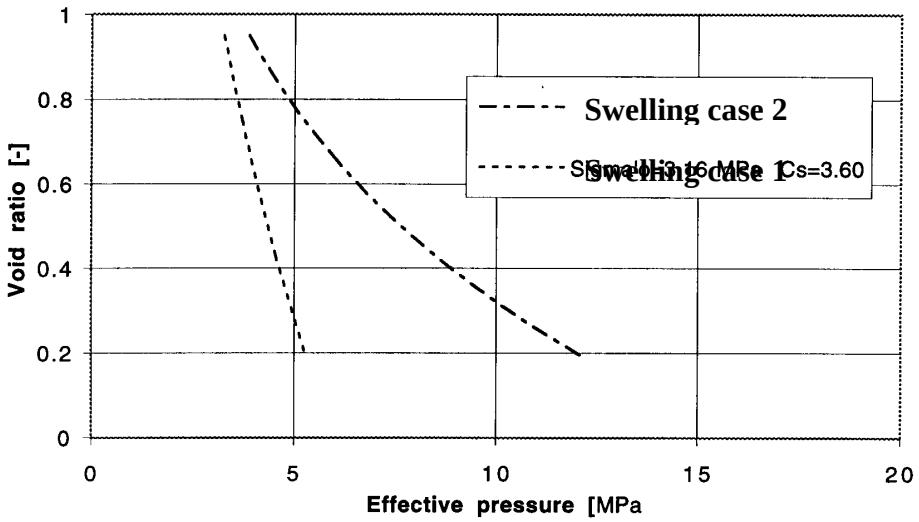

Figure 6.2 Effective stress as a function of the void ratio *e*.

Concerning the initial void ratio, commercial bentonite has usually a porosity of 30%, corresponding to a void ratio of 0.43. We will do a sensitivity analysis for the two following cases:

$e_0 =$ 0.43 (porosity n=30%),

0.11 (porosity n=10%).

The void ratio at the tip would have to be determined experimentally. We will use the following values:

$e_{limit} =$ 1.0, 2.7, 5.0, 8.0, 10.0.

There are no sensitivity studies on the initial canister radius

R_0=1 m.

6.2 SENSITIVITY TO THE HYDRAULIC CONDUCTIVITY AND COEFFICIENT OF SWELLING

All parameters are taken equal to their reference values, except for the hydraulic conductivity and the coefficient of swelling.

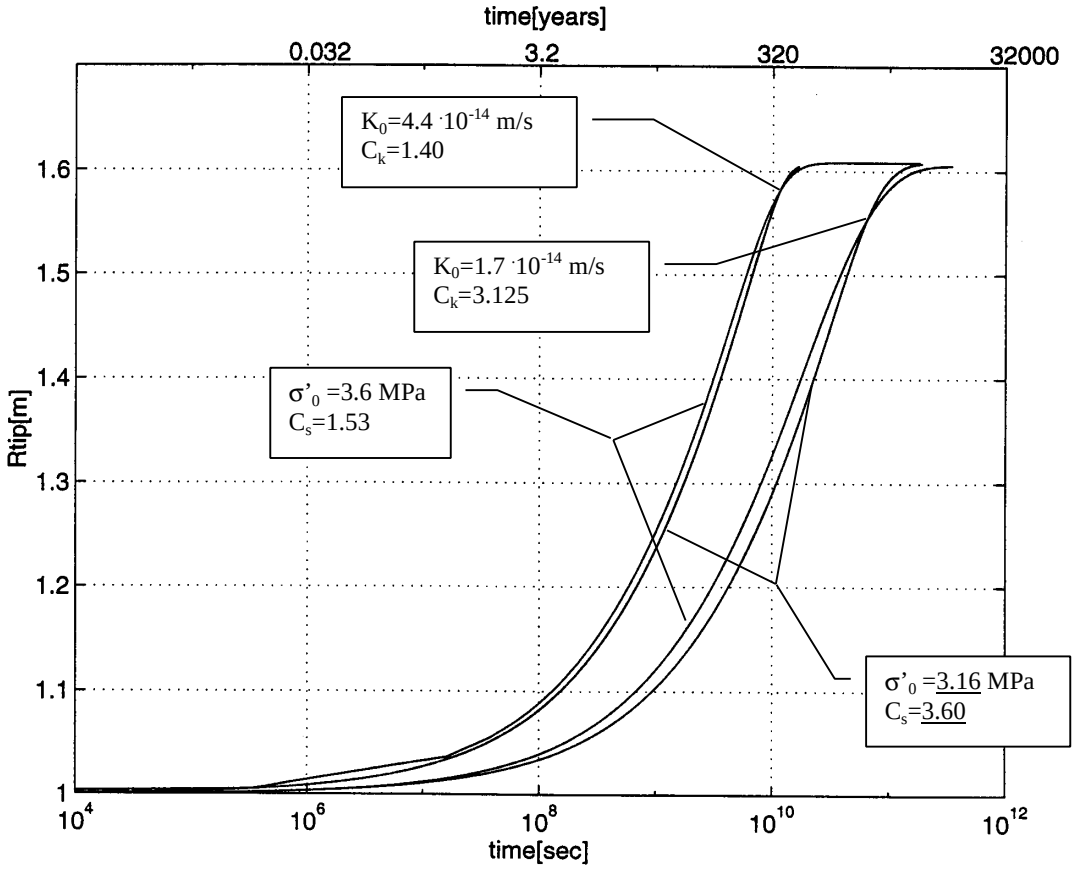

Figure 6.3 Sensitivity to the hydraulic conductivity and coefficient of swelling. Tip position as a function of time.

The time to reach stationary state is larger when the hydraulic conductivity is lower. On the other hand, this time is not much influenced by the coefficient of swelling.

6.3 SENSITIVITY TO THE INITIAL VOID RATIO

All parameters are taken equal to their reference values, except for the initial void ratio, which takes the value 0.43 and 0.11 corresponding to an initial porosity of 30 % and 10% respectively.

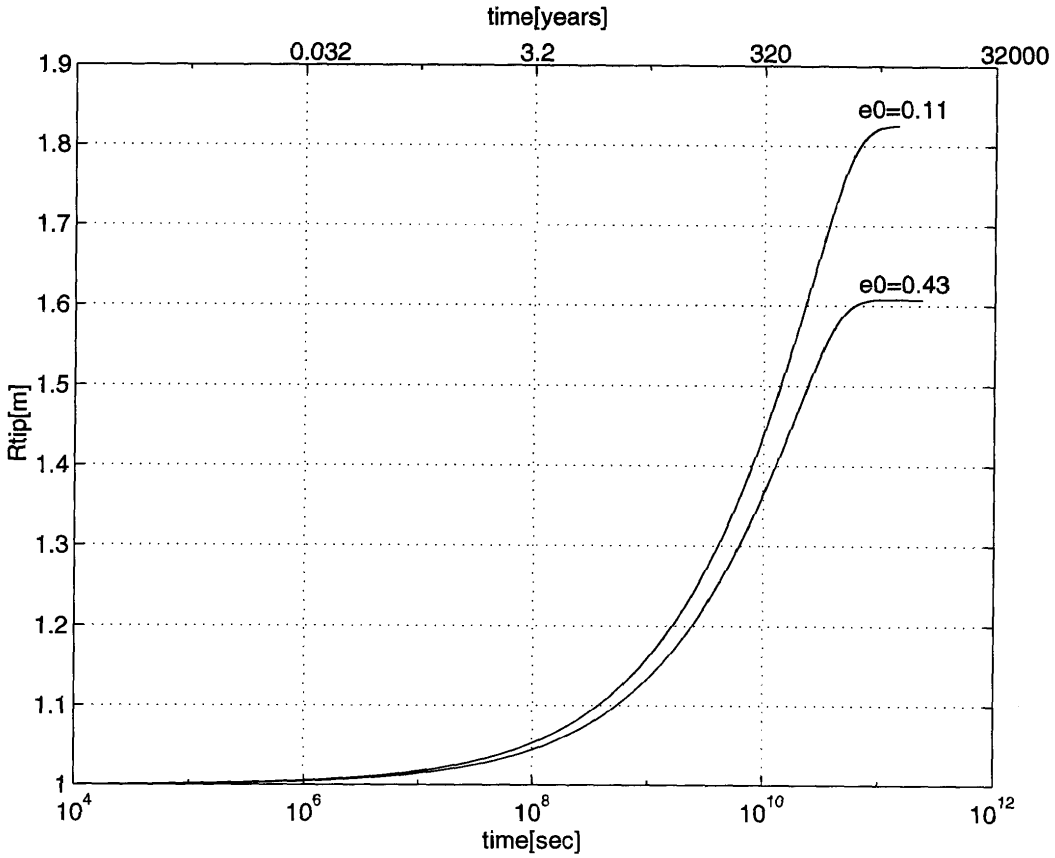

Figure 6.4 Sensitivity to the initial void ratio. Tip position as a function of time for different e_0.

The time to reach stationary state is not much influenced by the initial void ratio or porosity.

6.4 SENSITIVITY TO THE VOID RATIO AT THE TIP

The assumption that the void ratio at the tip is constant is a hypothesis, which has to be verified experimentally. The motivation for this sensitivity study is to observe the effect of void ratio variations on the time scale and on the void ratio radial distribution. In Figure **6.5**, the parameters are taken equal to their reference values, except for the void ratio at the tip, which vary from *1.0* to *10.0*. In Figures **6.6** and **6.7**, the void ratios at the tip are equal to 2.7 and 10.0 respectively, and the initial void ratio is equal to 0.11 (porosity=10%).

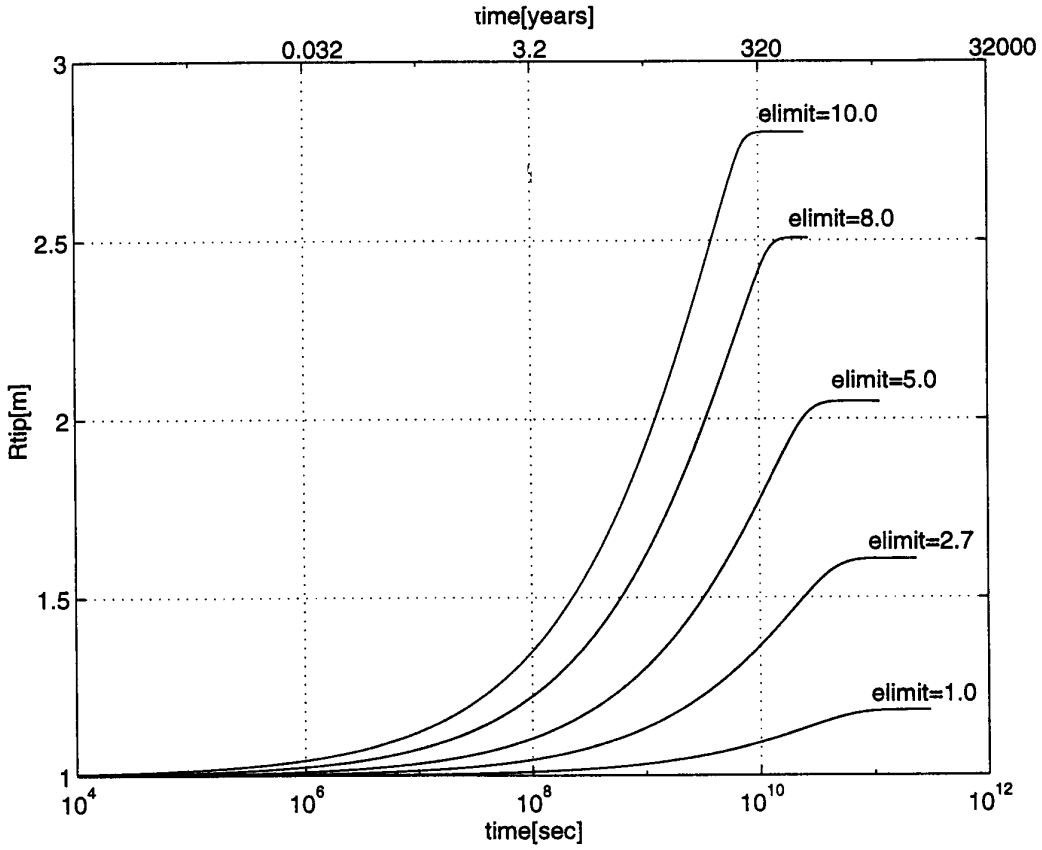

Figure 6.5 Sensitivity to the void ratio at the tip. Tip position as a functi on of time for different e_{limit}.

The time to reach stationary state is smaller for higher void ratios at the tip. It appears in Figure **6.7** that a region with very high void ratio emerges in front as the time increases.

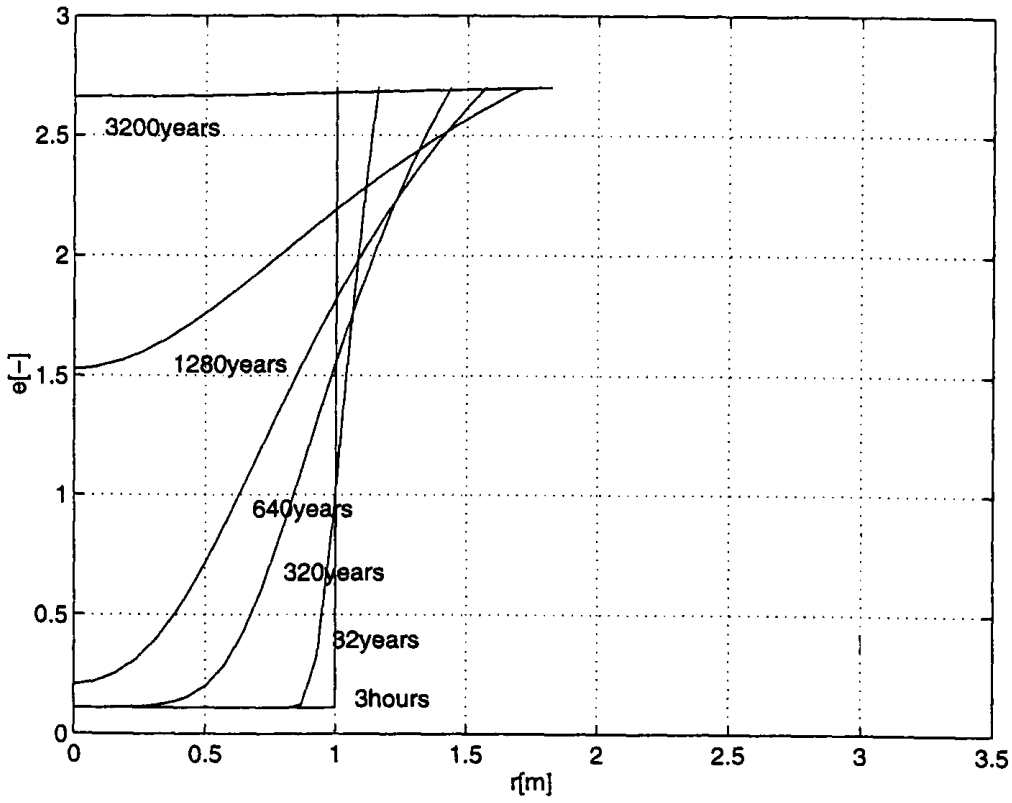

Figure 6.6 Sensitivity to the void ratio at the tip. Void ratio as a function of radius for e_{limit}=2.7.

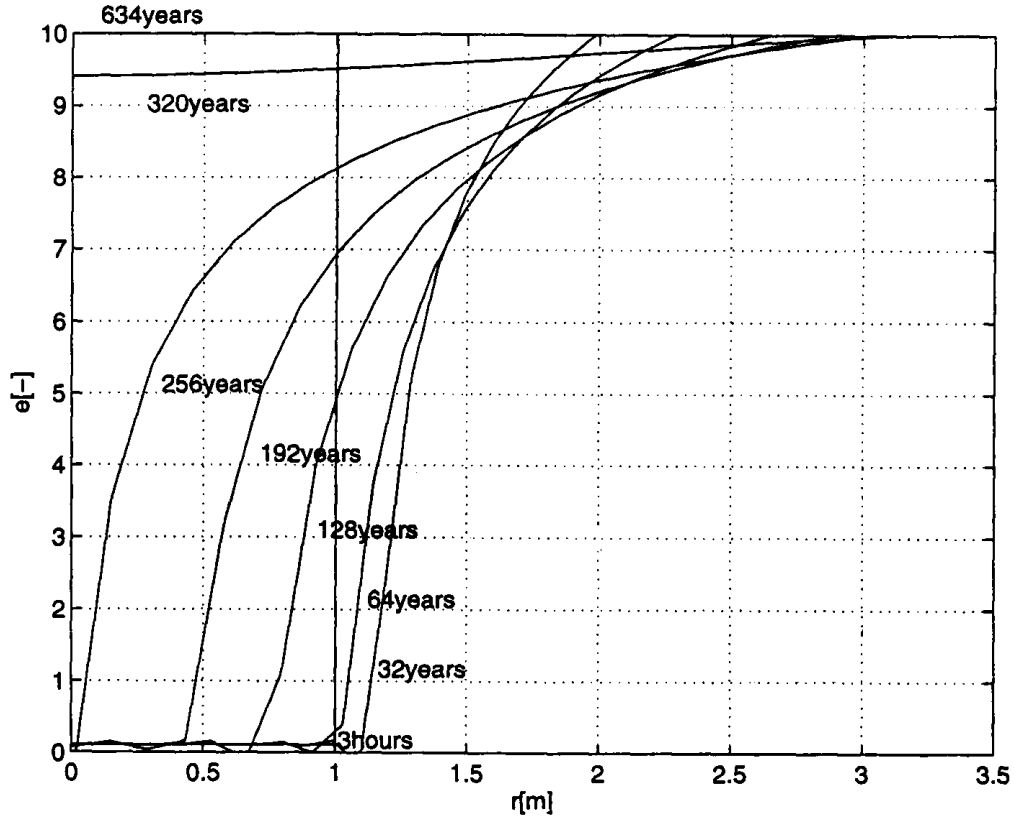

Figure 6.7 Sensitivity to the void ratio at the tip. Void ratio as a function of radius fo r e_{limit}=10.0.

6.5 DISCUSSION ON THE NUMERICAL RESULTS

The bentonite will completely expand in less than 3000 years. This has an important implication on the performance assessment of the engineered barriers. To get a better idea of the validity of our model, we have to study how the model differs from the reality. We will analyze successively all the assumptions that we introduced so far.

Saturation processes are not accounted for in our model because the bentonite is assumed to be initially saturated. If air-filled pores are present in the bentonite, some of them will absorb water while no swelling will be observed. The time required to fill up these pores should thus be added to the expansion time.

The bentonite may absorb more water if the fracture is completely filled with water at all times than if the amount of water supplied to the fracture per unit time is limited. In the latter case, bentonite expansion would be slower.

Side-fractures to the main fracture may be present and supply water to the bentonite sidewise. On the contrary to the first effects analyzed, this will decrease the expansion time.

Our model did not take into account the shear stresses against the walls of the fractures. Although they would probably not affect considerably the expansion of the bentonite for large fracture widths, shear-stresses should be considered for narrower fractures as they would retard bentonite expansion.

Figure **7.1** represents a case where a large cylindrical bentonite volume has to swell through a narrow fracture intersecting it. In this case, the water will start diffusing in this large volume not only radially but also vertically, acting as a sink for water. This will increase the void ratio gradient at the tip, increasing simultaneously the expansion rate. However, as more material has to be expelled out of the initial canister, the time to reach stationary state will be longer.

Assumption of the model	Effect on the time to reach the stationary stage if not fulfilled
Saturation	↑
No limit on the water supplied through the fracture	↑
No water supply to the sides of the fracture	↓
No shear stresses on the walls of the fracture	↑
The whole volume of bentonite expands radially	↑
Fixing the e_{limit}	↑ or ↓

Table 6.3 Effect of the assumptions on the time to reach stationary state.

This brief analysis seems to show that the expansion would take longer in a real repository. However, this result should be checked experimentally.

6.6 REFERENCES FOR CHAPTER 6

[1] R. Pusch, *Waste Disposal in Rock*, Elsevier, 1994.

[2] J.K. Mitchell, *Fundamentals of soil behavior*, Wiley, 1993.

CHAPTER
SEVEN

CONCLUSION

7.1 SUMMARY OF THIS STUDY

In the first part of this study, we surveyed the literature to find a model for bentonite swelling. Microscopic mechanisms for bentonite swelling were studied but neither the electrical double-layer theory [1] nor the recently proposed hydration layer theory [2] gave a complete mechanistic explanation for clay swelling. Based on Terzaghi's consolidation theory [3], a macroscopic model could be established for the expansion of bentonite by water absorption.

In the second part, amass conservation and Darcy's laws [4] are used to establish the governing equations for bentonite swelling. The exact geometry of the bentonite extrusion through the fractures is described and side-conditions of the problem are proposed. Regarding the clay properties, the permeability and effective pressure are characterized as functions of the void ratio. A literature survey provided us with common analytical expressions for these quantities where a few parameters are to be chosen to fit the experimental measurements.

In the third part, the bentonite expansion through a horizontal fracture is simulated with a time-dependent numerical algorithm. The basic algorithm is based on a fully implicit Galerkin/Finite Element technique on deforming elements combined with a predictor-corrector scheme. By combination of the predictor and the corrector, the temporal accuracy can be controlled by automatic time step modification. In order to validate our theoretical model, we derived an analytical expression for the bentonite expansion in a cylindrical geometry based on Terzaghi's consolidation theory [5].The comparison of the results shows an overall good agreement. Some numerical simulations have been performed to study the sensitivity of the expansion to the permeability, effective pressure, initial void ratio and void ratio at the tip.

7.2 CONCLUSION

Using some realistic data found in the literature for the material properties, the results of this model seem to show a rather fast expansion, i.e. of the order of 3000 years. Performance assessment of geologic repositories is usually based on the assumption that the bentonite engineered barrier will last forever. The relatively short expansion time found here will certainly have a considerable impact on performance assessment. With a longer travel time from the waste form to the bentonite/rock interface, previous studies [6] showed indeed that the concentrations of americium, plutonium and neptunium would reduce to negligible levels within the bentonite buffer region if the environment is

reducing. The total radioactive hazard outside of this buffer region would thus decrease to very low levels. On the downside of this swelling, the integrity of the buffer material as an engineered barrier could be affected by the loss of bentonite.

7.3 FUTURE WORK

It has to be noticed that this study has been performed without considering the initial unsaturated state of the bentonite, nor the shear stresses on the walls of the fractures, which would retard the bentonite swelling. Thus, the present model should be refined to account for these effects. A two-dimensional model which would account for shear stresses could be established based on a mass conservation and two momentum conservation equations. As a matter of fact however, before going on further refinements of the present model, it should be validated by comparison with some experiments close to the case studied theoretically. Also, more accurate measurements of the swelling pressure as a function of the void ratio would be necessary to validate the boundary conditions used in the model.

7.4 REFERENCES FOR CHAPTER 7

[1] J.K. Mitchell, *Fundamentals of Soil Behaviour*, 2nd ed., Wiley, New York, 1993.

[2] P.F. Low, *Interparticle Forces in Clay Suspensions: Flocculation, Viscous Flow and Swelling*, Proc. 1989 Clay Min. Soc. Workshop on Rheology of Clay/Water Systems, 1992.

[3] K. Terzaghi, *The Influence of Elasticity and Permeability on the Swelling of Two-Phase Systems*, Colloid Chemistry, Vol. III, Chemical Catalog Co., New York, pp. 65-88, 1931.

[4] H. Darcy, *Détermination des lois d'écoulement de l'eau à travers le sable.* Les fontaines publiques de la ville de Dijon, pp. 590-594. Paris : Victor Dalmont, 1856.

[5] K. Terzaghi, Erdbaumechanik auf bodenphysikalischer Grundlage, Leipzig und Wien, F. Deuticke, 1925.

[6] J.Ahn, P.L. Chambré, B. Light, D. Roberts, J. Verbeke, *Radioactive Transport in Disturbed Zone Between Engineered and Natural Barriers of Deep Geologic Disposal of High-Level Radioactive Wastes*, UCB-NE 4217, 1996.